Title

GROWTH on S190814bv: Deep Synoptic Limits on the Optical/Near-infrared Counterpart to a Neutron Star-Black Hole Merger

Journal

Astrophysical Journal, 890(2)

ISSN

0004-637X

Authors

Andreoni, I
Goldstein, DA
Kasliwal, MM
et al.

Publication Date

2020-02-20

DOI

10.3847/1538-4357/ab6a1b

Peer reviewed

Draft version October 30, 2019
Typeset using LaTeX **twocolumn** style in AASTeX62

GROWTH on S190814bv: Deep Synoptic Limits on the Optical/Near-Infrared Counterpart to a Neutron Star–Black Hole Merger

Igor Andreoni[1] and Daniel A. Goldstein[1,*]
these authors contributed equally to this work
Mansi M. Kasliwal,[1] Peter E. Nugent,[2,3] Rongpu Zhou,[2] Jeffrey A. Newman,[4] Mattia Bulla,[5,6] Francois Foucart,[7] Kenta Hotokezaka,[8] Ehud Nakar,[9] Samaya Nissanke,[10,11] Geert Raaijmakers,[10,11] Joshua S. Bloom,[3,2] Kishalay De,[1] Jacob E. Jencson,[1,12] Charlotte Ward,[13] Tomás Ahumada,[13] Shreya Anand,[1] David A. H. Buckley,[14] Maria D. Caballero-García,[15] Alberto J. Castro-Tirado,[16,17] Christopher M. Copperwheat,[18] Michael W. Coughlin,[1] S. Bradley Cenko,[19,20] Mariusz Gromadzki,[21] Youdong Hu,[16,22] Viraj R. Karambelkar,[1] Daniel A. Perley,[18] Yashvi Sharma,[1] Azamat F. Valeev,[23] David O. Cook,[24] U. Christoffer Fremling,[1] Harsh Kumar,[25] Kirsty Taggart,[18] Ashot Bagdasaryan,[1] Jeff Cooke,[26,27] Aishwarya Dahiwale,[1] Suhail Dhawan,[6] Dougal Dobie,[28,29] Pradip Gatkine,[13] V. Zach Golkhou,[30,31,†] Ariel Goobar,[6] Andreas Guerra Chaves,[10] Matthew Hankins,[1] David L. Kaplan,[32] Albert K. H. Kong,[33] Erik C. Kool,[34] Siddharth Mohite,[32,‡] Jesper Sollerman,[34] Anastasios Tzanidakis,[1] Sara Webb,[27,26] and Keming Zhang [3,‡]

[1] *California Institute of Technology, 1200 East California Blvd, MC 249-17, Pasadena, CA 91125, USA*
[2] *Lawrence Berkeley National Laboratory, 1 Cyclotron Road, Berkeley, CA 94720, USA*
[3] *Department of Astronomy, University of California, Berkeley, CA 94720-3411, USA*
[4] *Department of Physics and Astronomy and PITT PACC, University of Pittsburgh, PA, 15260, USA*
[5] *Nordita, KTH Royal Institute of Technology and Stockholm University, Roslagstullsbacken 23, SE-106 91 Stockholm, Sweden*
[6] *The Oskar Klein Centre, Department of Physics, Stockholm University, AlbaNova, SE-106 91 Stockholm, Sweden*
[7] *Department of Physics, University of New Hampshire, 9 Library Way, Durham NH 03824, USA*
[8] *Department of Astrophysical Sciences, Princeton University, Peyton Hall, Princeton, NJ 08544, USA*
[9] *Department of Astrophysics, Sackler School of Physics and Astronomy, Tel Aviv University, Tel Aviv, 69978, Israel*
[10] *GRAPPA, Anton Pannekoek Institute for Astronomy and Institute of High-Energy Physics, University of Amsterdam, Science Park 904, 1098 XH Amsterdam, The Netherlands*
[11] *Nikhef, Science Park 105, 1098 XG Amsterdam, The Netherlands*
[12] *University of Arizona, Steward Observatory, 933 N. Cherry Avenue, Tucson, AZ 85721, USA*
[13] *Department of Astronomy, University of Maryland, College Park, MD 20742, USA*
[14] *South African Astronomical Observatory, PO Box 9, Observatory 7935, Cape Town, South Africa*
[15] *Astronomical Institute, Academy of Sciences of the Czech Republic, Boční II 1401, CZ-141 00 Prague, Czech Republic*
[16] *Instituto de Astrofísica de Andalucía (IAA-CSIC), Glorieta de la Astronomía s/n, E-18008, Granada, Spain*
[17] *Departamento de Ingeniería de Sistemas y Automática, Escuela de Ingenieros Industriales, Universidad de Málaga, Unidad Asociada al CSIC, C. Dr. Ortiz Ramos sn, 29071 Málaga, Spain*
[18] *Astrophysics Research Institute, Liverpool John Moores University, IC2, Liverpool Science Park, 146 Brownlow Hill, Liverpool L3 5RF, UK*
[19] *Astrophysics Science Division, NASA Goddard Space Flight Center, MC 661, Greenbelt, MD 20771, USA*
[20] *Joint Space-Science Institute, University of Maryland, College Park, MD 20742, USA*
[21] *Astronomical Observatory, University of Warsaw, Al. Ujazdowskie 4, 00-478 Warszawa, Poland*
[22] *Universidad de Granada, Facultad de Ciencias Campus Fuentenueva S/N CP 18071 Granada, Spain*
[23] *Special Astrophysical Observatory, Russian Academy of Sciences, Nizhnii Arkhyz, 369167 Russia*
[24] *IPAC, California Institute of Technology, 1200 E. California Blvd, Pasadena, CA 91125, USA*
[25] *Indian Institute of Technology Bombay, Powai, Mumbai 400076, India*
[26] *Australian Research Council Centre of Excellence for Gravitational Wave Discovery (OzGrav), Swinburne University of Technology, Hawthorn, VIC, 3122, Australia*
[27] *Centre for Astrophysics and Supercomputing, Swinburne University of Technology, Hawthorn, VIC, 3122, Australia*
[28] *Sydney Institute for Astronomy, School of Physics, University of Sydney, NSW 2006, Australia*
[29] *CSIRO Astronomy and Space Science, P.O. Box 76, Epping, New South Wales 1710, Australia*
[30] *DIRAC Institute, Department of Astronomy, University of Washington, 3910 15th Avenue NE, Seattle, WA 98195, USA*

andreoni@caltech.edu

[31] The eScience Institute, University of Washington, Seattle, WA 98195, USA
[32] Center for Gravitation, Cosmology and Astrophysics, Department of Physics, University of Wisconsin–Milwaukee, P.O. Box 413, Milwaukee, WI 53201, USA
[33] Institute of Astronomy, National Tsing Hua University, Hsinchu 30013, Taiwan
[34] The Oskar Klein Centre & Department of Astronomy, Stockholm University, AlbaNova, SE-106 91 Stockholm, Sweden

ABSTRACT

On 2019 August 14, the Advanced LIGO and Virgo interferometers detected the gravitational wave (GW) signal S190814bv with a false alarm rate of 1 in 10^{25} years. The GW data indicated (with >99% probability) that the event had $M_1 \geq 5_\odot$ and $M_2 \leq 3M_\odot$, suggesting that it resulted from a neutron star–black hole (NSBH) merger (or potentially a low-mass binary black hole merger). Due to the low false alarm rate and the precise localization (23 deg^2 at 90%), S190814bv presented the community with the best opportunity yet to directly observe an optical/near-infrared counterpart to an NSBH merger. To search for potential counterparts, our collaboration (GROWTH) performed real-time image subtractions on 6 nights of public Dark Energy Camera (DECam) i- and z-band images that were acquired in the three weeks following the merger. The images covered >98% of the integrated probability area. Using a worldwide network of follow-up facilities, we systematically undertook spectroscopy and imaging of potential counterpart candidates discovered in the DECam data. Combining these data with a photometric redshift catalog that is >97% complete in the volume of interest, we ruled out each candidate as the counterpart to S190814bv. Here we present deep and uniform photometric limits on the optical emission associated with the event. For the nearest consistent GW distance, radiative transfer simulations of NSBH mergers constrain the ejecta mass of S190814bv to be $M_{\rm ej} < 0.04\ M_\odot$ at polar viewing angles, or $M_{\rm ej} < 0.03\ M_\odot$ if the opacity is $\kappa < 2$ cm^{2}g^{-1}. Assuming a tidal deformability for the neutron star compatible with GW170817 results, our limits would constrain the BH spin component aligned with the orbital momentum to be $\chi < 0.7$ for mass ratios $Q < 6$.

1. INTRODUCTION

Mergers of binaries containing neutron stars and stellar-mass black holes (NSBH mergers) have long been theorized as potential sites of r-process nucleosynthesis (Lattimer & Schramm 1974), that should be detectable by networks of laser interferometers as gravitational wave (GW) sources (Abadie et al. 2010), potentially harboring optical counterparts (Metzger & Berger 2012) that could be used to help constrain the equation-of-state (EOS) of dense nuclear matter (Geesaman 2015), measure the Hubble constant H_0 (Schutz 1986), and probe radiation hydrodynamics in asymmetric conditions and the limits of nuclear stability (Fernández & Metzger 2016). On 2019 August 14, the LIGO and Virgo interferometers detected S190814bv, the first high-confidence GW signal associated with an NSBH merger (The LIGO Scientific Collaboration and the Virgo Collaboration 2019a,b), confirming that NSBH mergers exist and that they produce gravitational waves.

Electromagnetic emission from NSBH mergers, which is critical to achieve many of the science goals described in the previous paragraph, is currently the subject of considerable theoretical uncertainty (e.g., Mingarelli et al. 2015; Hotokezaka & Nakar 2019; Barbieri et al. 2019). At this time, it is not clear whether optical/near-infrared (NIR) counterparts to NSBH mergers exist, and, if they do, what their properties might be. The uncertainty in the nature of electromagnetic counterparts to NSBH mergers is driven primarily by (1) uncertainties in the optical opacity of r-process elements in low ionization states, which may be the dominant opacity affecting spectrum synthesis in NSBH optical counterparts ("kilonovae," or "macronovae"), (2) a lack of knowledge regarding the EOS of dense nuclear matter, which directly affects the distribution of the merger ejecta and the post-merger nucleosynthesis, (3) an incomplete theoretical picture of the properties of NSBH matter outflows for all potential progenitor configurations, and (4) the complexity of the multiphysics simulations required to predict the observable properties of NSBH mergers, which at various stages must include sophisticated treatments of magnetohydrodynamics, General Relativity, neutrino transport, radiation transport, and nucleosynthesis.

* Hubble Fellow
† Moore-Sloan, WRF Innovation in Data Science, and DIRAC Fellow
‡ LSSTC Data Science Fellow

To help characterize the uncertain nature of electromagnetic emission from NSBH mergers, we present deep, synoptic, and red-sensitive limits on the optical/NIR emission from the NSBH merger S190814bv. We obtained the limits from public, multi-band observations of the localization region of S190814bv conducted by the Dark Energy Survey GW (DES-GW) collaboration (Soares-Santos et al. 2019a), who used the Dark Energy Camera (DECam, Flaugher et al. 2015) to tile >98% of the localization probability roughly 10 times in each of the i and z bands.

Section 2 gives an overview of the GW event and Section 3 describes the DECam follow-up. Our analysis methods are described in Section 4 and the results of follow-up observations of candidates of interest are presented in Section 5. In Section 6, we quantify the completeness of our galaxy catalogs. In Section 7, we use the limits obtained in the preceding analysis to constrain the ejecta mass, opacity, and viewing angle of S190814bv. The constraints on the ejecta mass are used to characterize the spin and the mass ratio of the progenitor binary. We summarize our results and present concluding remarks in Section 8.

2. S190814bv

The LIGO Scientific Collaboration and the Virgo Collaboration (2019a) detected the GW event S190814bv on 2019-08-14 21:10:39 UT, using four independent pipelines processing data from three GW interferometers (LIGO Hanford, LIGO Livingston, and Virgo) in triple coincidence. The false alarm rate of the event was 2×10^{-33} Hz, or approximately one in 10^{25} years. The GW event was first classified as "Mass Gap" with $> 99\%$ probability. A "mass gap" system refers to a binary where the lighter companion has mass $3M_\odot < M < 5M_\odot$, and no material is expected to be ejected. The classification of S190814bv was revised about 12 hours later (The LIGO Scientific Collaboration and the Virgo Collaboration 2019b) based on new parameter estimation obtained with the LALInference offline analysis pipeline (Veitch et al. 2015; Abbott et al. 2016) to an "NSBH" event with >99% probability. The refined analysis also indicated that there should be $< 1\%$ probability of having disrupted material surrounding the resulting compact object. In this work, we observationally probe the presence of remnant material that could generate an optical/NIR signature (see Section 7) and discuss the results in the context of the NSBH scenario.

LIGO/Virgo alerts with an "NSBH" classification refer to events in which the lighter object has $M \leq 3M_\odot$ and the heavier component has $M \geq 5M_\odot$. The maximum mass of a neutron star, according the most extreme viable EOS, is $M_{\rm ns,max} \approx 2.8M_\odot$ (Özel & Freire 2016). It is thus possible, given the LIGO/Virgo definition of "NSBH," that GW events classified as "NSBH" may actually be mergers of black holes having $M \geq 5M_\odot$ with lower-mass black holes having $M_{\rm ns,max} \leq M \leq 3M_\odot$. As the masses of the components of S190814bv are not yet public, we cannot yet comment on this possibility.

S190814bv was localized to 23 deg^2 at 90% confidence. For comparison, the binary neutron star (BNS) merger GW170817 was localized to 28 deg^2 (Abbott et al. 2017), then refined to 16 deg^2 (Abbott et al. 2019), and the three GW event candidates including neutron stars identified during O3 before S190814bv were localized to 7461 deg^2 (S190425z; The LIGO Scientific Collaboration & The Virgo Collaboration 2019a), 1131 deg^2 (S190426c; The LIGO Scientific Collaboration & The Virgo Collaboration 2019b), and 31 deg^2 (S190510g; LIGO Scientific Collaboration & Virgo Collaboration 2019), with S190510g having a significant probability of being non-astrophysical in origin. The precise localization of S190814bv is largely due to the fact that (1) it was detected with three GW interferometers and (2) it had a favorable location in the sky with respect to the antenna pattern of the detectors.

Despite the small localization area, the GW analysis places S190814bv at the fairly large distance of 267 ± 52 Mpc (The LIGO Scientific Collaboration and the Virgo Collaboration 2019b). This corresponds to a volume of 5.26×10^4 Mpc^3 for 90% area and 1σ distance, or a volume of 1.09×10^5 Mpc^3 for 90% area and 2σ distance. We focus the analysis presented in this paper to the 2σ volume, corresponding to the redshift range $0.037 < z < 0.081$.

3. DATASET

The initial "Mass Gap" classification made S190814bv a suitable candidate for follow-up with DECam under the NOAO program ID 2019B-0372 (PI Soares-Santos), which conducts observations of binary black hole (BBH) mergers, with the resulting data becoming immediately public. The program was triggered within a few hours of the merger, before the refined classification issued by The LIGO Scientific Collaboration and the Virgo Collaboration (2019b). The first exposure was taken roughly 7 hours after the merger at UTC 2019–08–15 06:32:43. Data were acquired on six distinct Chilean calendar nights (2019–08–14, 2019–08–15, 2019–08–16, 2019–08–17, 2019–08–20, and 2019–08–30), lasting from 1.5 to 4.5 hours each night. The moon and weather conditions steadily improved between the first and the last nights of the run, and the exposure times were more than twice as long in each filter at the end of the run than the

beginning, resulting in a greater achieved depth. Figure 1 shows the locations of the DECam exposures obtained during the run and processed in this analysis relative to the LALInference skymap of S190814bv.

4. METHODS

We processed the raw DECam data as they were taken, using the pipeline described in Goldstein et al. (2019), now running on the Amazon Web Services Elastic Compute Cloud (EC2) for increased reliability. For each exposure, a `c5.18xlarge` spot EC2 instance with 72 vCPUs and 144GB of RAM was launched to astrometrically and photometrically calibrate the DECam CCD images in parallel, make references, perform subtractions, identify candidates, filter them using `autoScan` (Goldstein et al. 2015), and perform aperture photometry. Each exposure took roughly 20 minutes to process, and the results were stored on the Amazon Simple Storage Service (S3). The median depths achieved nightly during the follow-up campaign with DECam are presented in Table 1.

4.1. *Photometric redshifts*

At the distance to S190814bv (∼250 Mpc), spectroscopic redshift catalogs are largely incomplete. We therefore relied primarily on photometric redshifts of transient host galaxies to assess whether transient candidates had distances consistent with the GW distance of S190814bv. We carried out an offline analysis of the DESI Legacy Imaging Surveys (Dey et al. 2019) Data Release 8 (DR8), which includes model-based photometry from the DECam and from the *Wide-field Infrared Survey Explorer* (*WISE*, Wright et al. 2010), to estimate photometric redshifts for the galaxies in the S190814bv localization region. By applying a Random Forest algorithm to the DR8 data (Zhou et al. 2019, in preparation), we generated a photometric redshift catalog for the entire DR8 footprint.

Due to its inclusion of data from Dark Energy Survey (DES, Dark Energy Survey Collaboration et al. 2016) observations, the catalog fully covered the S190814bv localization region. Catalogued sources with $m_z > 21$ were excluded because beyond that threshold the accuracy of the photometric redshifts rapidly degraded. As explained in Section 6, the impact of restricting our attention to candidates with potential host galaxies brighter than $z = 21$ has a negligible impact on our completeness, with an expected loss in luminosity fraction of $< 3\%$.

Sources with photometric redshift uncertainties $> 2\times$ the average photometric redshift uncertainty of all the sources of a similar magnitude within a 1 deg radius (± 0.1 mag) were also excluded as potential hosts. The distribution of photometric redshift uncertainties was estimated after rejecting stellar sources using a cut on the morphology of the best-fit light profile. We also rejected sources with *Gaia* parallaxes that are not compatible with 0 ± 1.081 mas obtained from the analysis of parallaxes measured for quasars (Luri et al. 2018). Spectroscopic redshifts (primarily from the 2dF Galaxy Redshift Survey, Colless et al. 2001) were considered instead of photometric redshifts when available.

4.2. *Candidate selection*

We used the GROWTH Marshal (Kasliwal et al. 2019) to display, filter, and assess candidates detected with our image-subtraction pipeline. During the scanning process, 519 candidates were saved that were located inside the 95% probability area of the skymap.

The candidates were cross-matched to known solar system objects from the IAU Minor Planet Center using the `astcheck`[1] utility. The cross-match radius between candidates and known solar system objects was $100''$. In addition to excluding known asteroids from our transient list, we identified elongated candidates (likely to be fast-moving uncatalogued solar system objects) by visual inspection and removed them.

The selection criteria for candidates to be reported in this work were defined as follows:

1. No match with moving objects reported in the IAU Minor Planet Center.
2. At least 2 detections in any filter with a time baseline of ≥ 30 minutes to further reject fast moving objects.
3. Location within the 95% probability contour of the LALInference skymap.
4. 2σ photometric or spectroscopic redshift confidence region (available before dedicated follow-up) of the possible host (requiring $m_z < 21$, see Section 4.1) consistent with the redshift range corresponding corresponding to the 2σ GW distance uncertainty from LIGO ($0.037 < z < 0.081$).
5. At least 3 detections with an `autoScan` score of 0.3 (to reject artifacts).
6. At least 10 DECam visits (including non-detections). Most coordinates on the skymap had at least 20 visits (see Figure 1).

[1] https://www.projectpluto.com/astcheck.htm

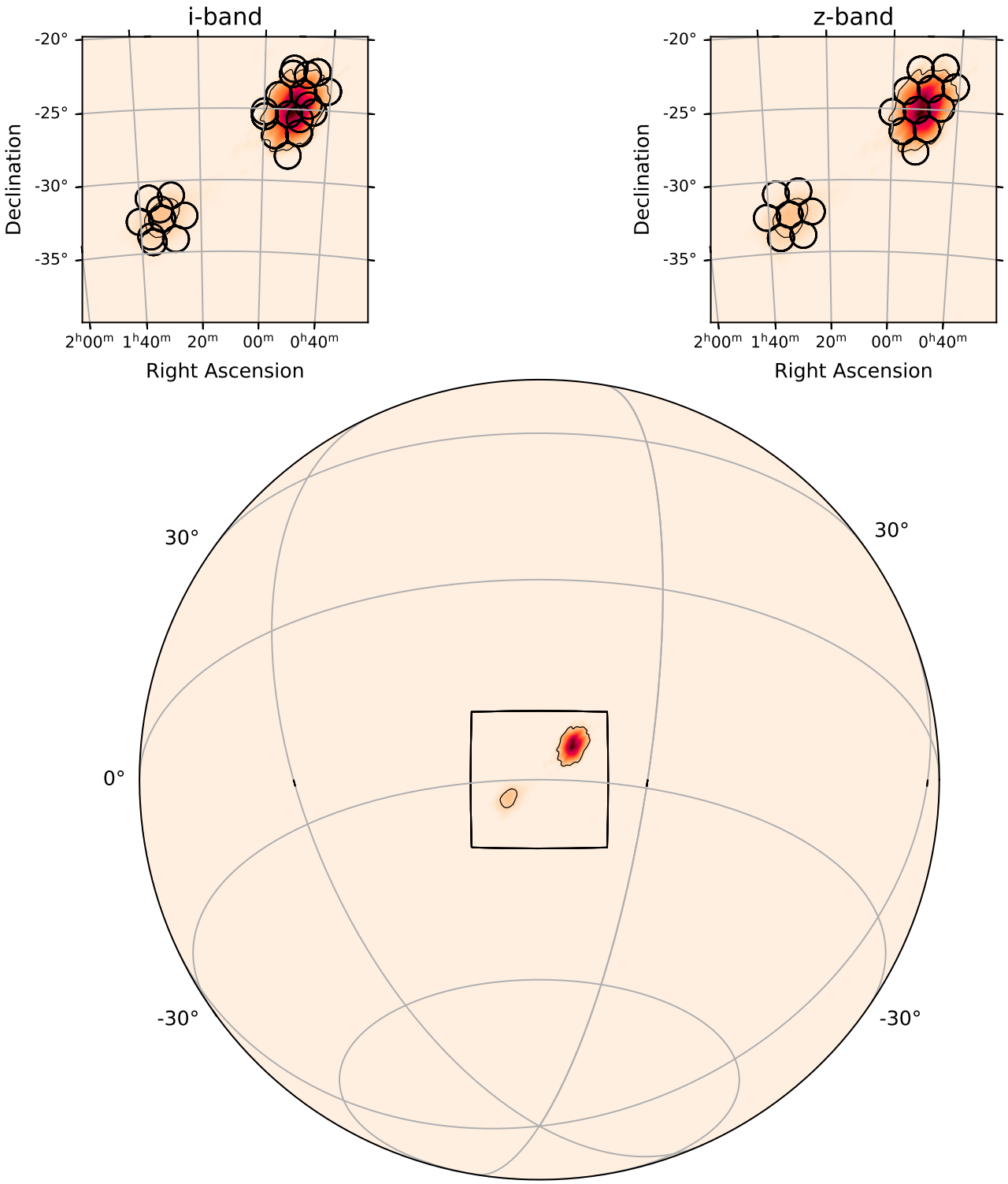

Figure 1. *Top row* – Locations of DECam exposures processed in this analysis (black circles) relative to the S190814bv LALInference skymap (The LIGO Scientific Collaboration and the Virgo Collaboration 2019b), with color linearly proportional to localization probability density. *Bottom row* – Bounding box of the top two plots (black square) relative to a global projection of the LALInference skymap.

Candidates discovered in real time were reported to the Transient Name Server[2] (TNS). New candidates (Andreoni et al. 2019; Goldstein et al. 2019b,a) and transient follow-up were reported via Gamma-ray Coordinates Network (GCN) circulars during the follow-up campaign. We used a radius of 20″ to cross-match our candidates with the photometric redshift catalog (see Section 4.1), which corresponds to a physical distance of 16 kpc at $z = 0.037$ and of 36 kpc at $z = 0.081$. A total of 21 candidates survived the cuts. The candidates passing the selection criteria are listed in Tables 2–3.

4.3. *Candidate follow-up methods*

The spectroscopic results presented in this paper include data obtained using Near Infrared Echellete Spectrometer (NIRES) and the Low Resolution Imaging Spectrometer (LRIS, Oke et al. 1995) at W. M. Keck Observatory. The NIRES data were reduced using the `Spextool` code (Cushing et al. 2004) adapted for NIRES. The LRIS data were processed using `lpipe`, the fully automated reduction pipeline for longslit spectroscopy described in Perley (2019). We observed three potential candidates with the 10.4m Gran Telescopio de Canarias (GTC, PI A. Castro-Tirado), located at the observatory of Roque de los Muchachos in La Palma (Canary Islands, Spain), equipped with the Optical System for Imaging and low-intermediate-Resolution Integrated Spectroscopy (OSIRIS, Cepa et al. 2000). GTC/OSIRIS spectra for the three targets were obtained either with the R1000B or with the R1000R grisms and a 1 arcsec slit covering the 3,700Å–7,500Å or 5,100Å–10,000Å range. The slit was placed in order to cover the candidate location and the host galaxy centre. Data were reduced and calibrated using standard routines. Optical images in the r-band filter were also taken for the candidates with GTC. Photometric zero points and astrometric calibration were computed using the Pan-STARRS catalogue (Chambers et al. 2016). We then performed point spread function (PSF) matching photometry of the targets. Spectroscopy of one candidate of interest was also obtained with 10m Southern African Large Telescope (SALT, Buckley et al. 2006, PI Buckley) equipped with the Robert Stobie Spectrograph (RSS, Burgh et al. 2003; Kobulnicky et al. 2003). The primary data reduction of the SALT/RSS spectra was done using the `PySALT` package (Crawford et al. 2010), which accounts for basic CCD characteristics (e.g., cross-talk, bias and gain correction) and cosmic ray removal. Standard `IRAF/Pyraf` routines were then used to undertake wavelength and relative flux calibrations. Due to the design of SALT, which has a changing field-dependent entrance pupil, spectrophotometric standard observations can only provide relative fluxes (Buckley et al. 2018).

The photometric evolution of the most promising candidates was monitored using the optical imaging component of the Infrared-Optical suite of instruments (IO:O) on the 2m Liverpool Telescope (LT, Steele et al. 2004) at Observatorio del Roque de los Muchachos. All images were processed with the LT IO:O pipeline and image subtraction was performed automatically using Pan-STARRS (Chambers et al. 2016) imaging as a reference, using the methods described in Fremling et al. (2016). Optical photometric follow-up data were also acquired using the Las Cumbres Observatory (LCO) telescope network under proposal ID 2019B-0244 (PI Coughlin). The LCO photometry was measured after subtracting reference images from the Legacy Surveys archive using the `HOTPANTS` package (Becker 2015). At infrared wavelengths we obtained photometry using the Wide-field Infrared Camera (WIRC, Wilson et al. 2003) on the Palomar 200-inch Hale telescope (P200). The P200/WIRC data were reduced using a reduction pipeline developed by members of our team (De et al., in preparation).

5. RESULTS

In this section, we describe the follow-up observations that were conducted to characterize each of the 21 objects that we selected as candidate counterparts to S190814bv using the methods described in Section 4. In addition, we discuss a selection of candidates that did not pass our selection criteria, but that were reported and extensively followed up in the first three weeks after S190814bv. Most of the objects presented individually were spectroscopically classified.

DG19qabkc/AT2019nqc—The candidate was first reported in Andreoni et al. (2019) and appeared to be $\sim 2''$ offset from its host galaxy. Although no spectroscopic redshift was available, the photometric redshift placed the host in the correct distance range (Goldstein et al. 2019b). The candidate was photometrically confirmed in the optical (Herner et al. 2019b; Dichiara et al. 2019b,c) and we detected the transient in the near infrared at magnitude $J \sim 21.4 \pm 0.2$ on 2019-08-18 using P200/WIRC (De et al. 2019d). A flux upper limit of $F < 2.9 \times 10^{-12}$ erg cm^{-2} s^{-1} (Evans et al. 2019) was placed using data acquired with the X–ray Telescope (XRT, Burrows et al. 2005) on the space-based *Neil Gehrels Swift Observatory*, hereafter referred to as *Swift*. We observed DG19qabkc/AT2019nqc with SALT/RSS starting on 2019-08-23 22:46:10 and two consecutive 1200 s exposures were obtained using the

[2] https://wis-tns.weizmann.ac.il

Average Date (UT)	Δt (days)	$m_{lim,i}$ 5σ-phot	$m_{lim,z}$ 5σ-phot	$m_{lim,i}$ detection limit	$m_{lim,z}$ detection limit	P_{enc} (i)	P_{enc} (z)	P_{enc} $(i+z)$
2019-08-15 08:18	0.46	21.1	20.9	20.4	20.3	92%	94%	94%
2019-08-16 07:57	1.45	21.8	22.0	21.0	21.1	97%	97%	98%
2019-08-17 06:59	2.41	22.3	22.3	21.3	21.4	97%	97%	98%
2019-08-18 07:32	3.43	22.9	22.9	22.1	22.3	97%	97%	98%
2019-08-21 06:21	6.38	23.4	23.2	22.8	22.6	93%	93%	94%
2019-08-31 06:11	16.37	24.2	···	23.4	···	63%	···	63%

Table 1. Median depth achieved during the follow-up of S190814bv. The dates correspond to the central time between the first and the last epoch acquired on each observing night, and Δt indicates the time lag from the merger time (The LIGO Scientific Collaboration and the Virgo Collaboration 2019a). The photometric depth corresponds to 5σ photometric magnitude limits (column 3 and 4) and detection depth indicates the detection limit of the image-subtraction pipeline. All magnitudes are calibrated to the AB system. The last three columns present the integrated probability of the S190814bv LALInference skymap observed on each observing night, with the last column considering the observations in both i and z filters.

PG300 transmission grating, which covered the spectral region 3300–9800Å. The seeing was $\sim 1.7''$ and a $1.5''$ slit was used, giving an average resolving power of ~ 370, or a resolution of ~ 18Å. A strong broad Hα line with a P-Cygni profile dominates the spectrum, with a weak Hβ line in absorption, consistent with a redshift of $z = 0.077$. A good match was obtained using SNID (Blondin & Tonry 2007) using SN2005cs, a SN type II, 14 days after maximum (Figure 2, see also Buckley et al. 2019). Our GTC/OSIRIS spectroscopic observations confirmed DG19qabkc/AT2019nqc to be a SN II at $z = 0.078 \pm 0.001$ (Lopez-Cruz et al. 2019a). We extensively monitored the transient with LCO and LT imaging. The photometry that we obtained (Table 5) confirms a slow evolution compatible with supernova behavior.

DG19wxnjc/AT2019npv—When the candidate was discovered (Goldstein et al. 2019a) it appeared to be offset from its host galaxy, the photometric redshift of which ($z = 0.072 \pm 0.056$) was compatible with the expected distance to S190814bv. The redshift of the host was spectroscopically measured to be $z = 0.056$ (Jonker et al. 2019). The candidate was later confirmed in the optical and near-infrared (Herner et al. 2019a; Smartt et al. 2019; Chen et al. 2019; Lipunov et al. 2019; Wang et al. 2019), but no X–ray counterpart was detected with *Swift*/XRT ($F < 3.8 \times 10^{-12}$ erg cm^{-2} s^{-1}, Evans et al. 2019) and no radio counterpart was detected with the Australian Square Kilometre Array Pathfinder (ASKAP) ($S_{943\mathrm{MHz}} < 75\,\mu$Jy; Dobie et al. 2019) and Karl G. Jansky Very Large Array (VLA) ($S_{6\mathrm{GHz}} < 12\,\mu$Jy; Mooley et al. 2019). Palmese et al. (2019) reported a possible archival detection in DES data, questioning the transient nature of DG19wxnjc/AT2019npv. Annis et al. (2019) produced precise photometry obtained with nightly stacks of DECam data, indicating the transient to be reddening at a rate $\Delta(i - z) \sim 0.05$ mag day^{-1}. The transient was also monitored photometrically with LCO and LT (see Coughlin et al. 2019, and Table 5), which produced detections in the r, i and z bands and a marginal detection $g \gtrsim 23.0$ on 2019-08-24 with LCO, further indicating the transient to be (or to have become) red in color. We obtained one epoch of P200/WIRC imaging of the transient in J band, and did not detect the source to a 5σ limit of 21.4 AB mag, although we caution that the photometry is contaminated by host galaxy light.

We obtained one NIR spectrum of DG19wxnjc with NIRES on the Keck II telescope on 2019 August 24 (De et al. 2019c,b). We acquired two sets of dithered ABBA exposures on the transient location for a total exposure time of 40 mins. The telluric standard HIP 7202 was used for flux calibration. The reduced and stacked spectra showed a largely featureless continuum between 1.0 and 2.5 μm (Figure 2) along with a prominent P-Cygni profile near 1.08 μm with an absorption velocity of ≈ 7000 km s^{-1}. This feature is consistent with He I at the redshift of the host galaxy, in addition to a weak hint for another He I feature at 2.05 μm, confirming the classification of this source as a Type Ib/c supernova and unrelated to S190814bv. Gomez et al. (2019) confirmed the SN Ib classification using the IMACS optical spectrograph on the Magellan telescope.

desgw-190814j/AT2019nxe—The candidate was announced by Soares-Santos et al. (2019c) and was independently detected with our image-subtraction pipeline on multiple z-band epochs with internal name DG19zcrpc. The photometric redshift of the host is $z = 0.106 \pm 0.035$. LCO photometry (Table 5) suggests no significant g-band evolution between 2019-08-22 and 2019-08-25 and color $r - i \simeq 0$ on 2019-08-22. The transient was observed with GTC in imaging and spectroscopy mode on 2019-08-23. The GTC/OSIRIS spectrum of desgw-190814j/AT2019nxe is compatible with

a SN Ia at redshift $z = 0.0777 \pm 0.0005$ (Castro-Tirado et al. 2019).

DG19rzhoc/AT2019num—We identified this candidate in DECam data (Goldstein et al. 2019a) and it was independently confirmed in the same dataset (Herner et al. 2019a), in images taken with the Reionization and Transients Infrared Camera (RATIR[3]) on the 1.5m Harold Johnson Telescope at the Observatorio Astronomico Nacional on Sierra San Pedro Martir (Dichiara et al. 2019a), and in VLT Survey Telescope (VST) images (Yang et al. 2019). We performed photometric follow-up with LCO and LT (Table 5) which revealed the transient to be slowly evolving on day timescales. A *Swift*/XRT upper limit was placed at $F < 4.1 \times 10^{-12}$ erg cm^{-2} s^{-1} (Evans et al. 2019). We obtained one epoch of P200/WIRC imaging of the source in J band and did not detect the source to a 5σ limit of 21.4 AB mag, although we caution that the transient location is contaminated heavily with host galaxy light. DG19rzhoc/AT2019num was spectroscopically classified as a Type II SN at redshift $z = 0.113$ using the Goodman High Throughput Spectrograph (GHTS) on the 4.1m Southern Astrophysical Research (SOAR) telescope (Tucker et al. 2019b).

PS19epf/AT2019noq—The candidate was identified with the Pan-STARRS1 telescope and reported on 2019-08-15 (Huber et al. 2019). We independently detected PS19epf/AT2019noq in DECam data starting on 2019-08-15 06:44:29 with internal name DG19lsugc. The transient was classified as SN II at redshift $z = 0.07$ using SOAR/GHTS (Rodríguez et al. 2019). A pre-detection of the transient in ZTF data 2 weeks before the GW event further excluded its association with S190814bv.

DG19wgmjc/AT2019npw—This candidate was discovered in DECam data (Andreoni et al. 2019) and flagged as a high priority target because of the photometric redshift of the putative host $z = 0.140 \pm 0.054$ being compatible with the distance of S190814bv (Goldstein et al. 2019b). The transient was confirmed with optical observations with other telescopes such as the Discovery Channel Telescope (DCT; Dichiara et al. 2019b,c), VST (Yang et al. 2019), and with our P200/WIRC imaging observations (De et al. 2019d). Photometric measurements on DECam data indicated no rapid optical evolution (Fremling et al. 2019). A *Swift*/XRT upper limit was placed at $F < 4.3 \times 10^{-12}$ erg cm^{-2} s^{-1} (Evans et al. 2019). DG19wgmjc/AT2019npw was eventually classified as a Type IIb SN at redshift $z = 0.163$ using SOAR/GHTS (Tucker et al. 2019b).

DG19sbzkc/AT2019ntr—We initially identified this candidate in DECam data (Goldstein et al. 2019a) and the detection was confirmed using RATIR (Dichiara et al. 2019a) and VST (Yang et al. 2019). We note that this transient did not pass the stricter selection criteria adopted in this work (see Section 4.2) because its location was visited 5 times, less than the 10-visit threshold that we imposed. DG19sbzkc/AT2019ntr was spectroscopically classified as a SN II at redshift $z = 0.2$ using SOAR/GHTS (Wiesner et al. 2019b).

desgw-190814q/AT2019obc—The candidate was found and announced by the DESGW team (Soares-Santos et al. 2019d) and we independently detected it with our automatic pipeline from 2019-08-16 05:56:59 with internal name DG19lkunc. Our DECam photometry using Pan-STARRS1 templates was consistent with a flat evolution until 2019-08-21 (Fremling et al. 2019). We acquired P200/WIRC near-infrared imaging in Ks band on MJD 58 717.492 and the transient was not detected down to a 5σ limit of $Ks > 20.72$ AB magnitude. desgw-190814q/AT2019obc was classified as a SN Ia few days past its peak at redshift $z = 0.216 \pm 0.005$ using GTC/OSIRIS (Castro-Tirado et al. 2019).

ZTF19abkfmjp/SN2019mbq—The transient was discovered with ZTF on 2019-07-30 (Nordin et al. 2019), before S190814bv, and it was classified as a SN II at redshift $z = 0.104 \pm 0.013$ with the SED Machine (Blagorodnova et al. 2018) on the 60-inch telescope at Palomar Observatory. We automatically found the transient (dubbed DG19fcmgc) in DECam data and it was also reported by two other groups via GCN (Soares-Santos et al. 2019a; Yang et al. 2019). Given the pre-detection with ZTF and the SN classification, ZTF19abkfmjp/SN2019mbq cannot be associated with S190814bv.

DG19gxuqc/AT2019paa—We obtained a spectrum of this nuclear candidate with Keck/LRIS. The spectrum was host-dominated, with common emission lines from the galaxy that allowed us to place the host at redshift $z = 0.191$, beyond the acceptable distance range for S190814bv.

All candidates in Table 3 are ruled out based on their photometric evolution being slower than 0.1 mag day^{-1}. This limit was adopted based on the photometric evolution of GW170817, the best-studied kilonova to date. GW170817 faded faster (almost 2 mag in g in 24 hours) and reddened faster (from $g - z = -0.3$ to $+1.3$ in 24 hours) than any known or theorized transient (e.g., Cow-

[3] www.ratir.org

perthwaite et al. 2017; Kilpatrick et al. 2017; Drout et al. 2017; Kasliwal et al. 2017). Theoretical models (e.g., Tanaka et al. 2018; Bulla 2019; Hotokezaka & Nakar 2019) also suggest that kilonovae arising from mergers with at least one NS are rapidly evolving transients. Requiring a photometric evolution faster than 0.1 mag/day to be considered a counterpart candidate is thus conservative, corresponding to evolution more than an order of magnitude slower than GW170817.

Other transients were published via GCN circulars, but were not reported in Table 2–3 because they did not pass our selection criteria or they were not detected with our pipeline. Soares-Santos et al. (2019b) published a complete list of candidates that they identified in DECam data in the first five nights of observations, including candidates identified in deep nightly stacks. In addition to a number of candidates already discussed in this section, we can associate only two more candidates to galaxies with photometric redshifts compatible with the distance to S190814bv. In particular, DG19zujoc/2019oac is located outside the 95% probability area of the LALInference skymap and desgw-190814z/AT2019omx did not have enough visits to pass our selection criteria (Section 4.2). In the available epochs, we do not measure any significant variability. Its photometric redshift of $z = 0.21 \pm 0.07$ passed our selection because we considered twice the uncertainties on photometric redshifts, however its large value suggests that the host galaxy is well beyond the distance range of interest.

Three DECam candidates DG19zoonc/AT2019nyy, DG19gyvx/AT2019thm, and DG19ggesc/AT2019paw lie within a 20″ radius from galaxies with photometric redshift compatible with S190814bv, however underlying galaxies at larger redshifts are most likely their host. DG19ggesc/AT2019paw is also coincident with a red stellar source detected with VISTA (Greggio et al. 2014). Therefore we exclude that DG19zoonc/AT2019nyy, DG19gyvx/AT2019thm, or DG19ggesc/AT2019paw are associated with S190814bv.

Two objects labelled desgw-190814a/AT2019nmd and desgw-190814b/AT2019nme were reported as transients possibly associated with S190814bv (Soares-Santos et al. 2019a). These candidates were followed up with several telescopes whose observations resulted in non-detections (McBrien et al. 2019; Huber et al. 2019; Belkin et al. 2019; Evans et al. 2019; Corre et al. 2019). Querying the IAU Minor Planet Center, we found that desgw-190814a/AT2019nmd is consistent with the known asteroid (297025) 2010 GA33 (De et al. 2019a). Inspection of DECam images allowed us to show that desgw-190814b/AT2019nme is a Solar System fast moving object (Goldstein et al. 2019) absent from the Minor Planet Center database. In conclusion, both desgw-190814a/AT2019nmd and desgw-190814b/AT2019nme were moving objects unrelated with S190814bv.

The transient labelled desgw-190814d/AT2019nqr was first reported by (Herner et al. 2019b). The candidate was detected twice with our automated pipeline (internal name DG19pihic), but the two detections occurred only 2.2 minutes apart on 2019-08-16, too close in time to pass our selection criteria of > 30 minutes between the first and last detection. desgw-190814d/AT2019nqr was later classified as a SN IIb using SOAR/GHTS (Tucker et al. 2019a).

The candidate desgw-190814c/AT2019nqq (Herner et al. 2019b; Tucker et al. 2019a; Goldstein et al. 2019b; De et al. 2019d; Herner et al. 2019a; D'Avanzo et al. 2019; Dichiara et al. 2019a) was automatically detected with our pipeline (dubbed DG19kxqic), but it was not included in Table 2 because it lies outside the LALInference 95% probability area of S190814bv. desgw-190814c/AT2019nqq was classified as SN II at $z = 0.071 \pm 0.001$ using GTC/OSIRIS (Lopez-Cruz et al. 2019b).

Other two candidates were reported, namely desgw-190814f/AT2019nte (Herner et al. 2019a) and desgw-190814r/AT2019odc (Soares-Santos et al. 2019b). Follow-up observations were performed for both candidates, fixing the redshifts of their putative host galaxies to $z = 0.054 \pm 0.001$ for desgw-190814r/AT2019odc (as part of our GTC/OSIRIS observations, Hu et al. 2019) and $z = 0.0702$ from the 2dF Galaxy Redshift Survey. However, both candidates did not pass the quality and reliability checks in our pipeline, in agreement with the non-detection of transient signatures in the spectra.

Four additional candidates that were detected with our pipeline were spectroscopically classified as SNe. The photometric redshift of their putative hosts placed them beyond the distance range for S190814bv. In particular, the spectrum of DG19rtekc/AT2019ntn (Goldstein et al. 2019a) obtained with SOAR/GHTS is consistent with a SN Ia-CSM or a SN IIn at $z = 0.1$ (Rodríguez et al. 2019); the GTC/OSIRIS spectrum of desgw-190814v/AT2019omt (Soares-Santos et al. 2019b) is consistent with a SN II at $z = 0.1564 \pm 0.0005$ (Hu et al. 2019); DG19gcwjc/AT2019ntp (Goldstein et al. 2019a) was classified as a broad-line SN Ic with SOAR/GHTS (Wiesner et al. 2019a); finally, the candidate desgw-190814e/AT2019nqs (Herner et al. 2019b; Dichiara et al. 2019b) was classified as a Type Ia or Type Ibc SN at redshift $z = 0.1263$ using the X-shooter instrument on the Very Large Telescope (VLT; Bruun et al. 2019).

In summary, none of the transients unveiled during this follow-up campaign appears to be a viable electromagnetic counterpart to the NSBH merger S190814bv.

Table 2. Subset of candidates discovered or independently detected by the DECam-GROWTH team during the follow-up of S190814bv that were spectroscopically classified. The reported candidates passed the selection criteria described in Section 4.2. Specifically, they lie within the 95% probability region of the LALInference skymap and are within 20″ from galaxies whose redshifts (2σ uncertainty) are compatible with the LIGO/Virgo distance (2σ). All the transients reported in this table were detected using the image-subtraction pipeline described in Section 4. [*] We note that DG19sbzkc was observed with < 10 visits and was added to this table for completeness.

Name	IAU Name	RA [deg]	Decl. [deg]	Offset [″]	spec-z	Classification	References
DG19qabkc	AT2019nqc	22.265296	−32.705155	2.2	0.078 ±0.001	SN II	Andreoni et al. (2019); Buckley et al. (2019); Lopez-Cruz et al. (2019a); Herner et al. (2019b); Dichiara et al. (2019b); Goldstein et al. (2019b); De et al. (2019d); Dichiara et al. (2019c); Evans et al. (2019); D'Avanzo et al. (2019)
DG19wxnjc	AT2019npv	13.384653	−23.832918	2.1	0.056	SN Ibc	Goldstein et al. (2019a); De et al. (2019b); Gomez et al. (2019); Herner et al. (2019a); Evans et al. (2019); Jonker et al. (2019); Smartt et al. (2019); Chen et al. (2019); Annis et al. (2019); Fremling et al. (2019); De et al. (2019c); Palmese et al. (2019); Dobie et al. (2019); Lipunov et al. (2019); Coughlin et al. (2019); Mooley et al. (2019); Gomez et al. (2019); Wang et al. (2019)
desgw-190814j	AT2019nxe	11.570153	−24.372559	1.9	0.0777	SN Ia	Soares-Santos et al. (2019c); Castro-Tirado et al. (2019); Soares-Santos et al. (2019b)
DG19rzhoc	AT2019num	13.881677	−22.969021	1.9	0.113	SN II	Goldstein et al. (2019a); Herner et al. (2019a); Evans et al. (2019); Dichiara et al. (2019a); Fremling et al. (2019); Tucker et al. (2019b); Corre et al. (2019); Yang et al. (2019)
PS19epf	AT2019noq	12.199507	−25.306523	5.0	0.07	SN II	Huber et al. (2019); Rodríguez et al. (2019)
DG19wgmjc	AT2019npw	13.968326	−25.783301	1.3	0.163	SN IIb	Andreoni et al. (2019); Dichiara et al. (2019b); Goldstein et al. (2019b); De et al. (2019d); Dichiara et al. (2019c); Herner et al. (2019a); Evans et al. (2019); Fremling et al. (2019); Tucker et al. (2019b); Corre et al. (2019); Yang et al. (2019)
DG19sbzkc*	AT2019ntr	15.007883	−26.714390	11.6	0.2	SN II	Goldstein et al. (2019a); Goldstein & Anand (2019); Dichiara et al. (2019a); Soares-Santos et al. (2019b); Wiesner et al. (2019b); Corre et al. (2019); Yang et al. (2019)

Table 2 continued

Table 2 *(continued)*

Name	IAU Name	RA [deg]	Decl. [deg]	Offset [″]	spec-z	Classification	References
desgw-190814q	AT2019obc	14.566689	−24.139699	1.4	0.216 ±0.005	SN Ia	Soares-Santos et al. (2019d); Fremling et al. (2019); Soares-Santos et al. (2019b); Castro-Tirado et al. (2019)
ZTF19abkfmjp	SN2019mbq	10.835364	−25.883974	1.0	0.104 ± 0.013	SN II	Soares-Santos et al. (2019a); Yang et al. (2019)

Table 3. Additional candidates discovered during the follow-up of S190814bv whose host galaxy redshift is compatible with the LIGO/Virgo distance (2σ). These candidates are ruled out based on photometric evolution. The reported candidates passed the selection criteria described in Section 4.2.

Name	IAU Name	RA [deg]	Decl. [deg]	Offset [″]	$z_{\rm phot}$	σ_z	$\langle m_i - m_z \rangle$	$\langle \dot{m}_i \rangle$ [mag/day]	$\langle \dot{m}_z \rangle$ [mag/day]
DG19aferc	AT2019tig	14.517916	−26.083013	0.08	0.074	0.03	···	−0.01	···
DG19gxuqc	AT2019paa	13.807414	−24.119017	0.40	0.116	0.06	0.01	−0.09	0.09
PS19ekf[a]	AT2019nbp	11.739110	−24.361751	0.42	0.102	0.01	−0.18	0.01	0.03
DG19hqhjc	AT2019nuj	12.257212	−23.234668	0.25	0.074	0.12	0.01	−0.01	0.00
DG19ilqnc	AT2019tih	11.861086	−27.600835	14.41	0.217	0.08	···	0.03	···
DG19kpykc	AT2019nul	13.818560	−26.943068	0.44	0.095	0.01	−0.23	−0.07	−0.09
DG19tedsc	AT2019tii	12.396721	−27.035924	0.21	0.055	0.03	···	···	···
DG19wynuc	AT2019tij	12.232094	−22.393476	0.32	0.157	0.11	0.43	−0.06	−0.02
DG19bpkf	AT2019tiw	15.022907	−24.950557	0.70	0.218	0.07	···	0.01	···
DG19bown	AT2019tix	12.190325	−24.647386	4.27	0.190	0.07	−0.14	0.02	0.01
DG19ggesc	AT2019paw	12.142854	−25.090528	19.47	0.285	0.13	0.23	0.00	0.03
DG19zoonc	AT2019nyy	12.069377	−26.640810	11.52	0.212	0.07	···	···	−0.01
DG19gyvx	AT2019thm	11.985939	−26.900779	18.73	0.233	0.09	···	···	···

[a] DG19hcsgc, with Pan-STARRS1 pre-discovery on 2019-08-09

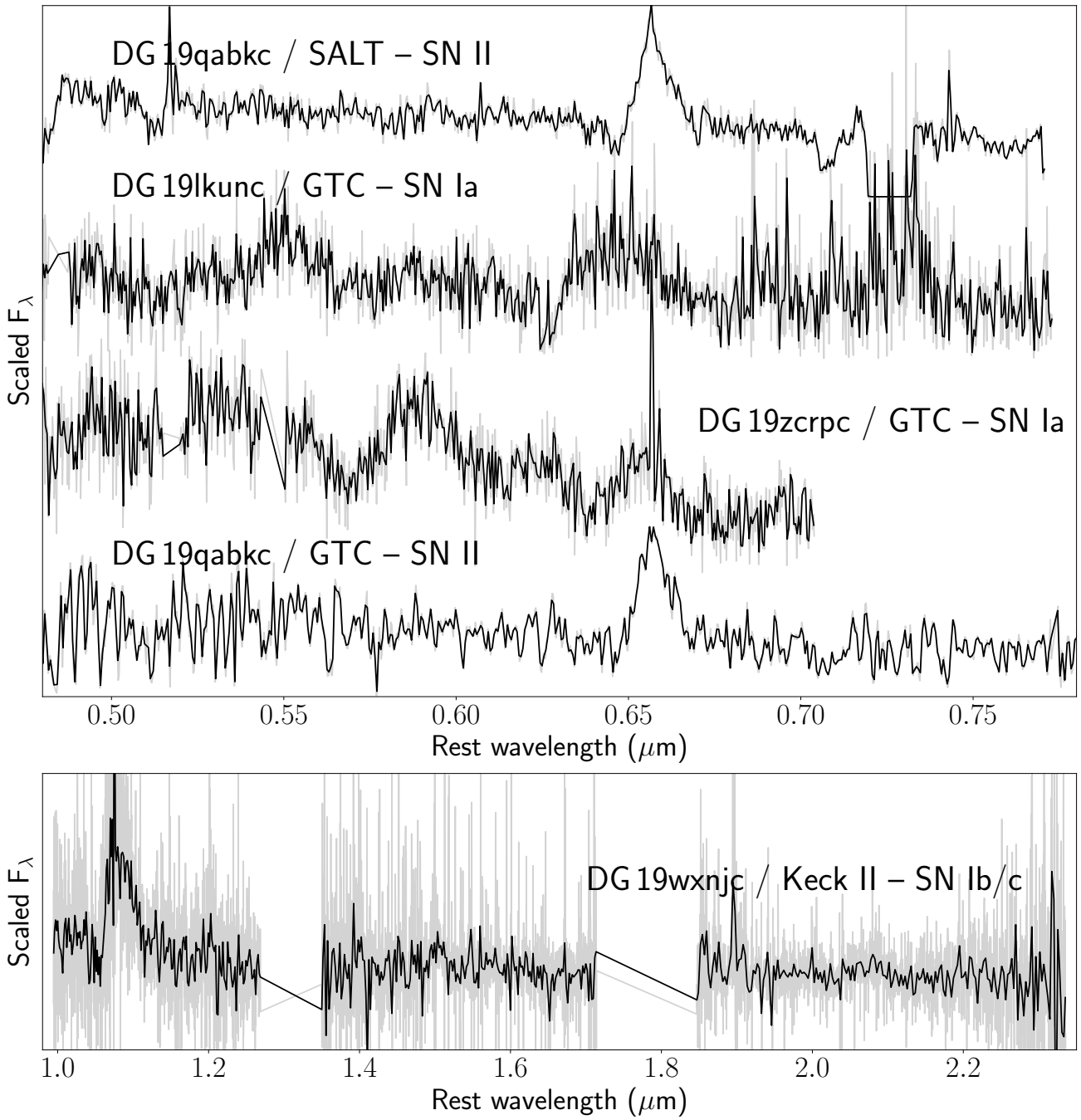

Figure 2. *Top panel* – Optical spectroscopic follow-up of candidates found in the localization region. The black lines correspond to binned versions of the unbinned reduced spectra shown in gray. GTC / OSIRIS and SALT spectra of DG 19qabkc show a strong P-Cygni Hα line suggesting a Type II supernova at $z = 0.08$. GTC / OSIRIS spectra of DG19lkunc and DG19zcrpc are consistent with SNe Ia at $z = 0.21$ and $z = 0.08$ respectively. *Lower panel* – Near-infrared spectrum of DG19wxnjc obtained with Keck II / NIRES. The spectrum shows a prominent P-Cygni feature at $\approx 1.08\mu$m, consistent with He I with an absorption velocity of 7000 km s^{-1}, classifying this source as a Type Ib/c supernova. These classifications rule out associations of these sources to S190814bv.

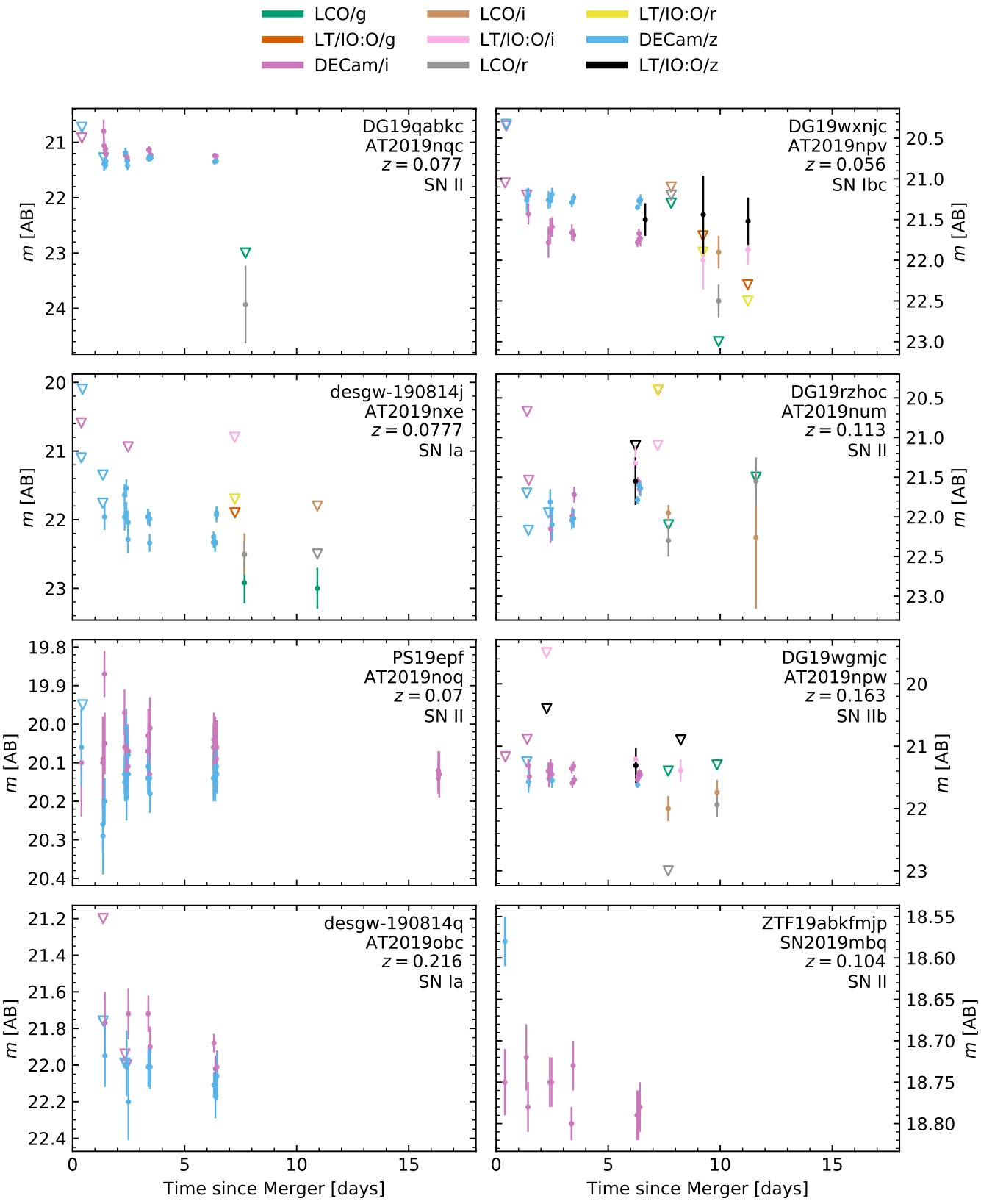

Figure 3. Light curves of all candidates presented in Table 2. The LCO and LT photometry upper limits are quoted to 3σ, while DECam upper limits are quoted to 5σ. P200/WIRC photometry was not plotted because it is host contaminated. For the transient PS19epf/AT2019noq, one measurement among the 6 available on day 16 was excluded.

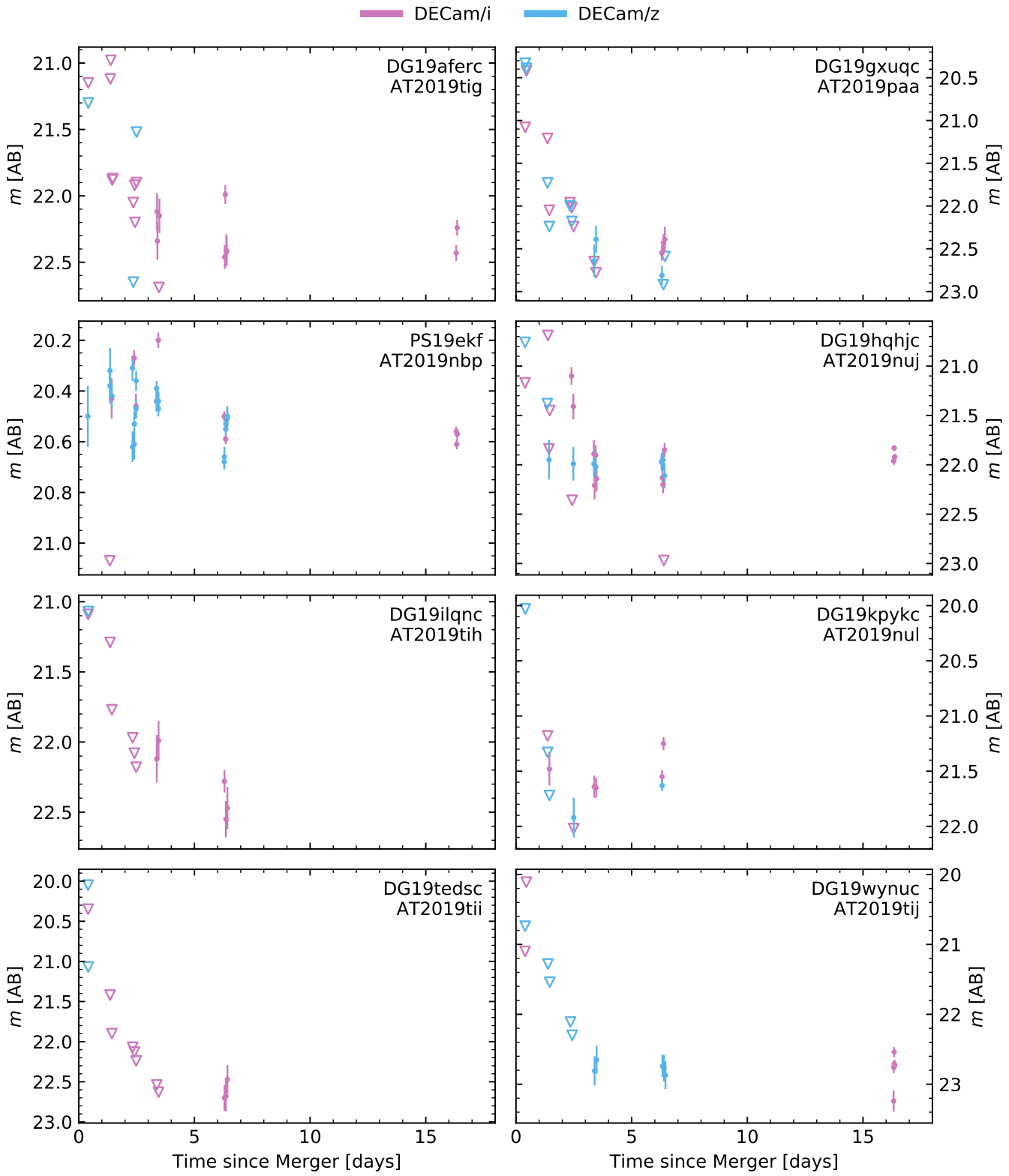

Figure 4. DECam light curves of eight of the thirteen candidates presented in Table 3. Light curves of the remaining five candidates are shown in Figure 5.

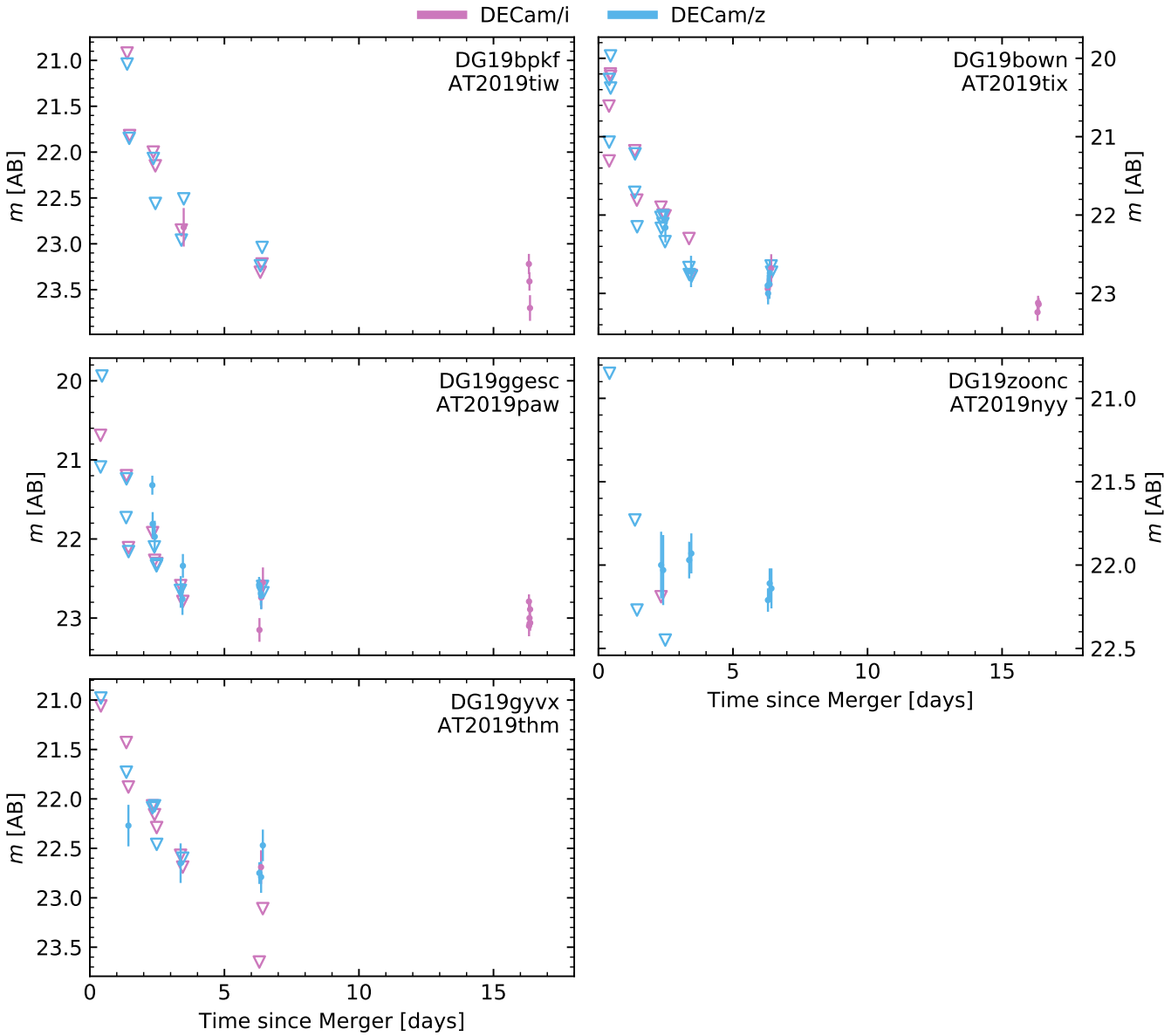

Figure 5. Light curves of the last five candidates presented in Table 3. The light curves of the other candidates in Table 3 are shown in Figure 4.

Table 4. Photometry of DECam candidates with LCO/IO:O, LT, and P200/WIRC. The LCO and LT photometry upper limits are quoted to 3σ, while DECam upper limits are quoted to 5σ. P200/WIRC photometry was obtained without image subtraction, thus the measurements are affected by host contaminations. The light curves are plotted in Figure 3.

Name	IAU Name	Date	Telescope	Filter	m (AB)	σ_m	$m_{\rm lim}$
DG19qabkc	AT2019nqc	2019-08-17	LT	–	–	–	–
		2019-08-18 11:15	P200/WIRC	J	21.4	0.2	–
		2019-08-20	LT/IO:O	–	–	–	–
		2019-08-21	LT/IO:O	–	–	–	–
		2019-08-22 14:27:08	LCO	g	–	–	23.0
		2019-08-22 14:27:08	LCO	r	23.93	0.7	–
		2019-08-23	LT/IO:O	–	–	–	–
		2019-08-25	LT/IO:O	–	–	–	–
DG19wxnjc	AT2019npv	2019-08-21 11:22:33	P200/WIRC	J	–	–	21.4
		2019-08-21 12:57:36	LT/IO:O	z	21.5	0.2	–
		2019-08-22 16:41:46	LCO	g	–	–	21.3
		2019-08-22 16:41:46	LCO	r	–	–	21.2
		2019-08-22 16:41:46	LCO	i	–	–	21.1
		2019-08-24 02:41:42	LT/IO:O	g	–	–	21.7
		2019-08-24 02:48:54	LT/IO:O	r	–	–	21.9
		2019-08-24 02:56:06	LT/IO:O	i	22.0	0.36	–
		2019-08-24 03:03:10	LT/IO:O	z	21.44	0.48	–
		2019-08-24 19:28:04	LCO	g	–	–	23
		2019-08-24 19:28:04	LCO	r	22.5	0.2	–
		2019-08-24 19:28:04	LCO	i	21.9	0.2	–
		2019-08-26 02:39:50	LT/IO:O	g	–	–	22.3
		2019-08-26 02:47:02	LT/IO:O	r	–	–	22.5
		2019-08-26 02:54:14	LT/IO:O	i	21.87	0.18	–
		2019-08-26 03:01:26	LT/IO:O	z	21.52	0.29	–
desgw-190814j	AT2019nxe	2019-08-22 02:49:21	LT/IO:O	i	–	–	20.8
		2019-08-22 02:59:36	LT/IO:O	r	–	–	21.7
		2019-08-22 03:09:48	LT/IO:O	g	–	–	21.9
		2019-08-22 13:16:38	LCO	g	22.92	0.3	–
		2019-08-22 13:16:38	LCO	r	22.51	0.2	–
		2019-08-22 13:16:38	LCO	i	22.5	0.3	–
		2019-08-25 19:22:23	LCO	g	23.0	0.3	–
		2019-08-25 19:22:23	LCO	r	–	–	22.5
		2019-08-25 19:22:23	LCO	i	–	–	21.8
DG19rzhoc	AT2019num	2019-08-21 02:19:24	LT/IO:O	i	21.32	0.22	–
		2019-08-21 02:25:09	LT/IO:O	z	21.55	0.3	–
		2019-08-21 02:28:05	LT/IO:O	z	–	–	21.1
		2019-08-21 11:39:50	P200/WIRC	J	–	–	21.4*
		2019-08-22 02:14:28	LT/IO:O	i	–	–	21.1
		2019-08-22 02:24:41	LT/IO:O	r	–	–	20.4
		2019-08-22 02:34:52	LT/IO:O	g	–	–	20.4
		2019-08-22 13:44:36	LCO	g	–	–	22.1

Table 4 continued

Table 4 *(continued)*

Name	IAU Name	Date	Telescope	Filter	m (AB)	σ_m	$m_{\rm lim}$
		2019-08-22 13:44:36	LCO	r	22.3	0.2	–
		2019-08-22 13:44:36	LCO	i	21.95	0.1	–
		2019-08-26 11:30:44	LCO	g	–	–	21.5
		2019-08-26 11:30:44	LCO	r	21.55	0.3	–
		2019-08-26 11:30:44	LCO	i	22.26	0.9	–
DG19wgmjc	AT2019npw	2019-08-17 03:08:01	LT/IO:O	i	–	–	19.5
		2019-08-17 03:16:41	LT/IO:O	z	–	–	20.40
		2019-08-18 11:15:00	P200/WIRC	J	21.2	0.18*	–
		2019-08-21 02:41:05	LT/IO:O	i	21.21	0.2	–
		2019-08-21 02:49:45	LT/IO:O	z	21.31	0.28	–
		2019-08-22 13:30:42	LCO	g	–	–	21.4
		2019-08-22 13:30:42	LCO	r	–	–	23.0
		2019-08-22 13:30:42	LCO	i	22.0	0.2	–
		2019-08-23 02:49:51	LT/IO:O	i	21.39	0.18	–
		2019-08-23 02:58:31	LT/IO:O	z	99.0	99.0	20.9
		2019-08-24 17:48:21	LCO	g	–	–	21.3
		2019-08-24 17:48:21	LCO	r	21.94	0.2	–
		2019-08-24 17:48:21	LCO	i	21.74	0.2	–
desgw-190814q	AT2019obc	2019-08-18 11:15:00	P200/WIRC	Ks	–	–	20.7

[*] Photometry obtained without image subtraction

6. GALAXY CATALOG COMPLETENESS

The completeness of a synoptic follow-up campaign such as the one conducted with DECam for S190814bv is mainly limited by the area covered and the efficiency of the transient detection pipeline. Once these two quantities are set, the ability to detect an EM counterpart becomes flux limited. Given a mean detection limit of 21.7 mag (Table 1), we were able to find transients with absolute magnitude $M \leq -14.4$ at a distance $D = 163$ Mpc, $M \leq -15.4$ at $D = 267$ Mpc, and $M \leq -16.1$ at $D = 371$ Mpc.

Several publications (for example, Nissanke et al. 2013; Singer et al. 2016; Gehrels et al. 2016) advocate that galaxy-targeted follow-up of GW triggers can be very effective when the event occurs within tens of megaparsecs. The discovery of AT2017gfo (the optical counterpart to GW170817) using a galaxy-targeted strategy is an example of success of this approach at a distance of 41 Mpc (Coulter et al. 2017). At distances beyond $\sim$ 200 Mpc, galaxy catalogs become more incomplete and, assuming a constant volumetric density, the number of galaxies per distance interval increases rapidly. Both these factors work disfavor galaxy targeted searches, the former because many uncatalogued galaxies at the distance of interest would be ignored, the latter because more telescope time (usually limited especially for large aperture telescopes) is required to image more galaxies at the same depth. Galaxy-targeted searches are also affected by a detection efficiency lower than 100% if image-subtraction techniques are applied, even more if they are not. Gomez et al. (2019) used the Magellan telescope to observe galaxies possibly hosting the S190814bv merger. In their work, Gomez et al. (2019) imaged 96 galaxies at 3σ magnitude limit $i < 22.2$, corresponding to $M_i = -14.9$ mag at 267 Mpc. The sample includes all galaxies in the GLADE catalog within the 50% probability volume with luminosity $\geq 0.15L^*$.

Here we estimate the completeness of a hypothetical galaxy-targeted follow-up campaign in the 90% probability volume compared with our DECam analysis. Assuming i) the same depth of the synoptic observations, ii) a similar transient detection efficiency, and iii) unlimited telescope time to observe all the cataloged galaxies in the distance range of interest, the completeness of a galaxy-targeted search would be directly dependent on the galaxy catalog completeness and on the properties of the catalogued galaxies. The completeness of the Galaxy List for the Advanced Detector Era (GLADE, Dálya et al. 2018) galaxy catalog compilation, calculated as integrated luminosity fraction over the 2σ redshift interval of S190814bv, is 5.5% (Figure 6). This completeness point corresponds to $B < 15.5$ (de Vaucouleurs et al. 1991; Corwin et al. 1994) for a Schechter function as in Gehrels et al. (2016), where $B = 15.5$ is

the magnitude at which the catalog is considered complete.

The analysis presented in this paper took advantage of photometric redshifts calculated from Legacy Surveys and *WISE* photometry mainly to exclude from our sample those candidates likely associated with galaxies significantly outside the distance range of S190814bv. Astrophysical transients with no clear association to a host galaxy were not excluded *a priori*, but their photometric evolution was not rapid enough for them to be considered likely counterparts to S190814bv. Nevertheless, we estimate the completeness that we could reach considering only a sample of transients found in the proximity of galaxies present in the photometric redshift catalog. Assuming a conservative limit of $B = 21$, we obtain a completeness $> 97\%$ based on the luminosity fraction in the 2σ distance range of S190814bv. Although it is likely that the $z < 21$ excludes a large number of small, faint galaxies with $z > 21$, we are still nearly complete in luminosity.

We note that z-band luminosity is a much better proxy for stellar mass than luminosity in bluer bands such as B, such that the spread in z band mass-to-light ratio is smaller than the range of B/z flux ratios amongst galaxies. As a result, the stellar mass completeness of the $z < 21$ subset of DECaLS would be expected to be at least as high as the conservative B luminosity completeness estimated here.

The completeness estimated above assumes conditions (i.e., unlimited telescope time) to observe all galaxies in a GW event's volume. However, this will rarely be the case for events similar to S190819bv. To provide a more realistic completeness given limited observing time, we can compute the number of galaxies needed to be observed in order to cover various luminosity fractions of galaxies. Figure 7 shows the cumulative B-band luminosity fraction for the 947 GLADE galaxies found in the 90% volume of S190819bv, where this distribution is normalized by 1) the total luminosity of the GLADE galaxies in this volume and 2) the total luminosity expected given a Schechter luminosity function (Gehrels et al. 2016). A galaxy-targeted observing strategy would have to observe 169 and 541 GLADE galaxies in order to cover the top 50% and 90% of the total luminosity, respectively. However, these numbers are significantly higher assuming that the completeness is better described by a Schechter luminosity function, where 307 galaxies are needed to cover 50% of the total luminosity and reaches a maximum of 70% if all GLADE galaxies are observed.

7. DISCUSSION

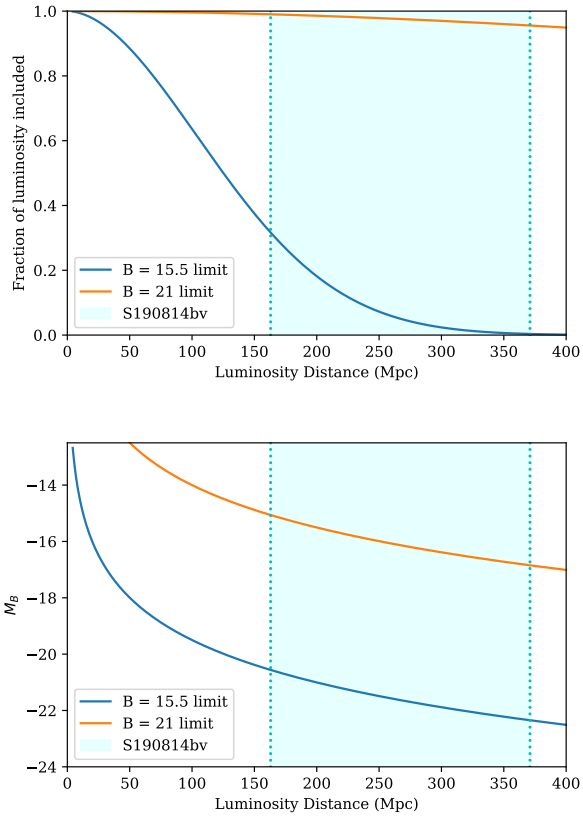

Figure 6. Luminosity fraction (*upper panel*) and B-band absolute magnitude limit (*lower panel*) as a function of luminosity distance. These quantities were estimated for the GLADE catalog (blue line) as well as for the Legacy Surveys DR8 photometric redshifts (orange line). The 2σ distance interval for S190819bv (The LIGO Scientific Collaboration and the Virgo Collaboration 2019b) is delimited by the cyan-colored dashed lines.

The results presented in Section 5 show that no viable counterpart to S190814bv was discovered. In this section we discuss the constraints that this non-detection places on the astrophysical properties of the merger.

7.1. *Kilonova models*

We used the upper limits obtained with DECam and kilonova simulations to constrain the parameter space of the possible EM counterpart to S190814bv. Specifically, we consider the kilonova models developed by Bulla (2019) and Hotokezaka & Nakar (2019).

We first compare DECam limits to 2D kilonova models computed with the Monte Carlo radiative transfer code POSSIS (Bulla 2019). These models assume a two-component ejecta geometry, with a lanthanide-rich component distributed around the equatorial plane and characterized by an half-opening angle ϕ and a lanthanide-poor component at higher latitudes (see Fig-

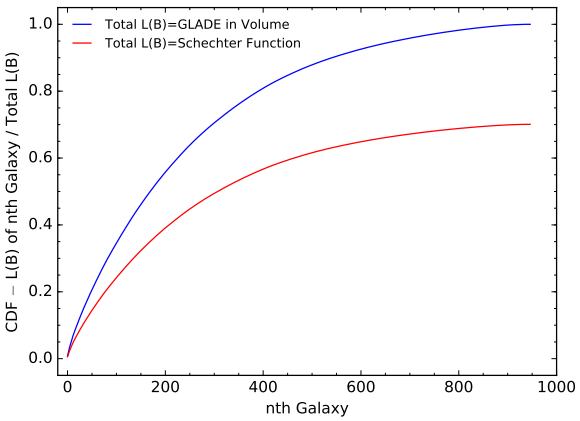

Figure 7. Cumulative luminosity fraction of GLADE galaxies in the S190819bv 90% volume normalized by 1) the total B-band luminosity of the GLADE galaxies in this volume (blue line), and 2) the total B-band luminosity expected given a Schechter function (red line) with parameters described in Gehrels et al. (2016).

ure 1 in Bulla et al. 2019). Radiative transfer calculations are then performed to predict spectral time series for 11 different viewing angles, from which broad-band light-curves can be easily extracted. For our analysis, we choose $\phi = 15°$ and $\phi = 30°$ guided by numerical simulations (Kawaguchi et al. 2016; Fernández et al. 2017) and calculate light curves for ejecta masses $M_{\rm ej}$ between 0.01 and 0.10 $M_\odot$ (step size 0.01 $M_\odot$).

The top panels of Figure 8 show which modelled light curves are ruled out by DECam $i-$band (left) and $z-$band (right) limits for different distance assumptions (215, 267 and 319 Mpc from light to dark blue). As expected, more models are brighter than the limits and thus ruled out at closer compared to farther distances. Interestingly, we find that the most constraining limit is the $z-$band point at 3.4 days (z=22.3 mag), with all the other limits bringing no improvement in terms of ruling out models. We note that comparable deep limits at earlier epochs, when the kilonova is intrinsically brighter, would have been extremely important to constrain the parameter space more strongly.

The bottom panels of Figure 8 show what region of the $M_{\rm ej}$ - viewing angle parameter space is ruled out for $\phi = 15°$ (left) and $\phi = 30°$ (right). The brightest kilonovae in the modelled grid are predicted at high $M_{\rm ej}$ and for polar viewing angles (system viewed face-on, $\theta_{\rm obs} = 0$ and $\cos\theta_{\rm obs} = 1$). These models are therefore the first to be ruled out by DECam limits (upper-right corner in the $M_{\rm ej}$ - viewing angle parameter space). Stronger constraints are found for closer distances (see above) and smaller ϕ angles as the larger contribution of the lanthanide-poor compared to lanthanide-rich component leads to an intrinsically brighter kilonova. We note that the best-fit model to GW170817 in this grid ($M_{\rm ej} = 0.05\ M_\odot$, $\phi = 30°$ and $\cos\theta_{\rm obs} = 0.9$, Dhawan et al. 2019) would be slightly fainter and thus hidden below DECam limits at 267 Mpc. To summarise, ejecta masses are constrained to $M_{\rm ej} < 0.04\ M_\odot$ in the most optimistic case assuming the nearest consistent distance of 215 Mpc, $\phi = 15°$ and $\cos\theta_{\rm obs} = 1$ (face-on). A more conservative constraint ($M_{\rm ej} \lesssim 0.10\ M_\odot$) is instead found for farther distances, viewing angles closer to the equatorial plane and larger ϕ values.

Figure 9 presents upper limits on the ejecta mass obtained using a different approach. We assume a spherical ejecta with a power-law density profile $\rho \propto v^{-n}$ for $v_{min} < v < v_{max}$ and calculate the emission using the heating rate formalism and light curve modeling described in Hotokezaka & Nakar (2019). The outflow parameters are $v_{min} = 0.1$c, $v_{max} = 0.4$c and $n = 4.5$. The composition that we consider is of r-process elements with atomic mass $85 \leq A \leq 209$ and a solar abundance pattern. The heating-rate calculation includes only β-decay. We assume further that the entire ejecta can be characterised by a single grey opacity parameter κ and vary the value of κ. The shaded regions in the M_{ej}-κ space in Figure 9 are where the light curve is brighter than the upper limits we have for this event. The conclusion from this figure is that the ejecta cannot have more than $\sim 0.05\ M_\odot$ of ejecta that is not lanthanide rich at a distance of 267 Mpc, or $\sim 0.03\ M_\odot$ at an optimistic distance of 215 Mpc. This conclusion is in agreement with the results obtained with the Bulla (2019) kilonova models under favorable ($\theta \lesssim 30°$) viewing angles.

7.2. *Constraints on the merging binary*

A constraint on the amount of mass ejected by the merger can be translated into constraints on the initial parameters of the merging objects. Given the mass ratio of the binary $Q = M_{\rm BH}/M_{\rm NS}$, the dimensionless component of the initial black hole spin aligned with the orbital angular momentum ($\chi_{\rm aligned}$), the compactness of the neutron star $C_{\rm NS} = GM_{\rm NS}/(R_{\rm NS}c^2)$, we have at our disposal analytical fits to the results of merger simulations that predict whether the neutron star disrupts before plunging into the black hole and, if disruption occurs, the mass $M_{\rm out}$ that remains outside of the black hole after merger (Foucart 2012; Foucart et al. 2018) with $\sim 15\%$ relative uncertainty. We also have an analytical fit predicting the amount of mass $M_{\rm dyn}$ ejected during disruption (Kawaguchi et al. 2016). Finally, we know that, conservatively, $\gtrsim 10\%$ of the matter initially bound in an accretion disk around the remnant

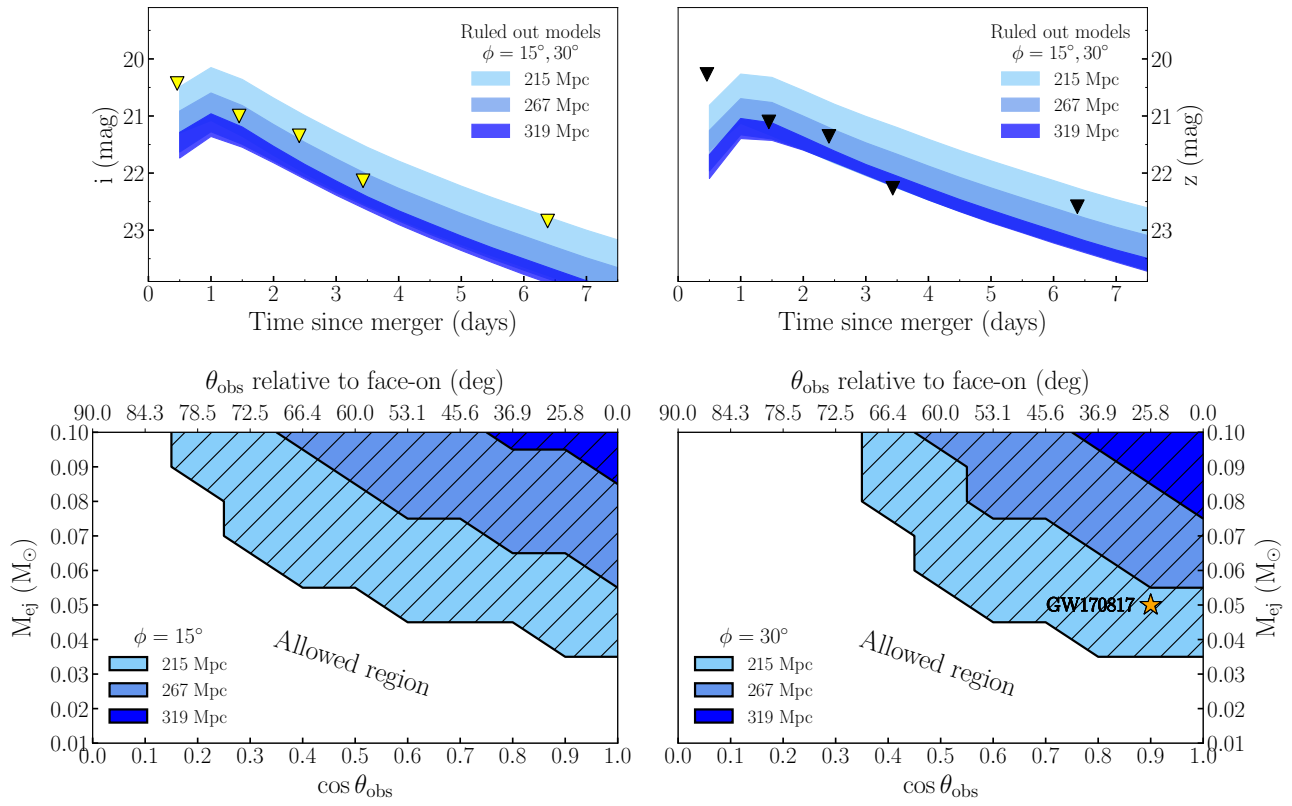

Figure 8. The limits obtained with DECam observations excluded regions of the parameter space for given kilonova models. In this figure we consider models obtained with the Monte Carlo radiative transfer code POSSIS (Bulla 2019) whose key parameters are the viewing angle θ_{obs}, the half-opening angle of an equatorial lanthanide-rich component ϕ, and the ejecta mass M_{ej}. *Top* – i (left) and z (right) band light curves of kilonovae ruled out using the multi-band DECam upper limits (Table 1), here marked with triangles. *Bottom* – Using the multi-band DECam upper limits, regions of the ejecta mass and viewing angle parameter space can be ruled out using $\phi = 15°$ (left) and $\phi = 30°$ (right). The best-fit model to GW170817 in this grid ($M_{ej} = 0.05\ M_\odot$, $\phi = 30°$ and $\cos\theta_{obs} = 0.9$, Dhawan et al. 2019) is marked with a yellow star in the right panel. Both the *top* and *bottom* plots show that constraints on the models are more stringent if lower distances to S190814bv are considered. Here we used distances of 319 Mpc (dark blue patches), 267 Mpc (light blue patches), and 215 Mpc (cyan patches).

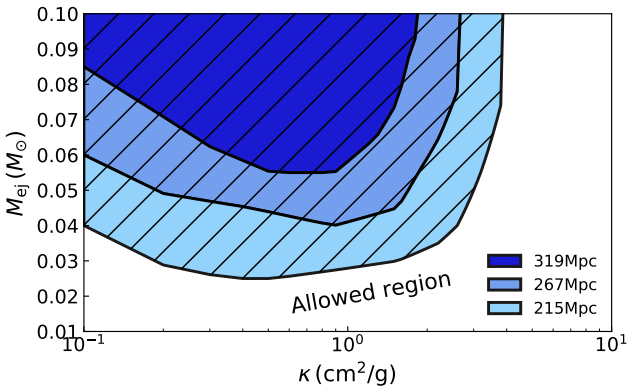

Figure 9. Constraints on the ejecta mass (M_{ej}) and opacity (κ) phase space obtained using multi-band DECam upper limits (Table 1) and the kilonova models described in Hotokezaka & Nakar (2019). Similarly to Figure 8, the constraints become more significant assuming lower distances to the merger.

black hole will be ejected in magnetically-driven and/or neutrino-driven winds, and during viscous expansion of the disk (Fernandez & Metzger 2013; Fernández et al. 2015; Siegel & Metzger 2017; Christie et al. 2019).[4] Accordingly, we make the conservative assumption that

$$M_{ej} \gtrsim M_{dyn} + 0.1(M_{out} - M_{dyn}). \quad (1)$$

In Figure 10, we show constraints on the parameter space of black hole-neutron star binaries assuming (a) $M_{ej} = 0.03 M_\odot$ and (b) $M_{ej} = 0.1 M_\odot$. We compute M_{out} as in Foucart et al. (2018), and M_{dyn} using a refit of the data presented in Kawaguchi et al. (2016), aiming at more physical behavior for compact neutron stars. Practically, an upper bound on M_{ej} can be interpreted

[4] For low mass black holes leaving remnants comparable to the initial conditions of existing 3D simulations, $\gtrsim 25\%$ of the disk is most likely ejected, but more compact disks around massive black holes eject a smaller fraction of their disk.

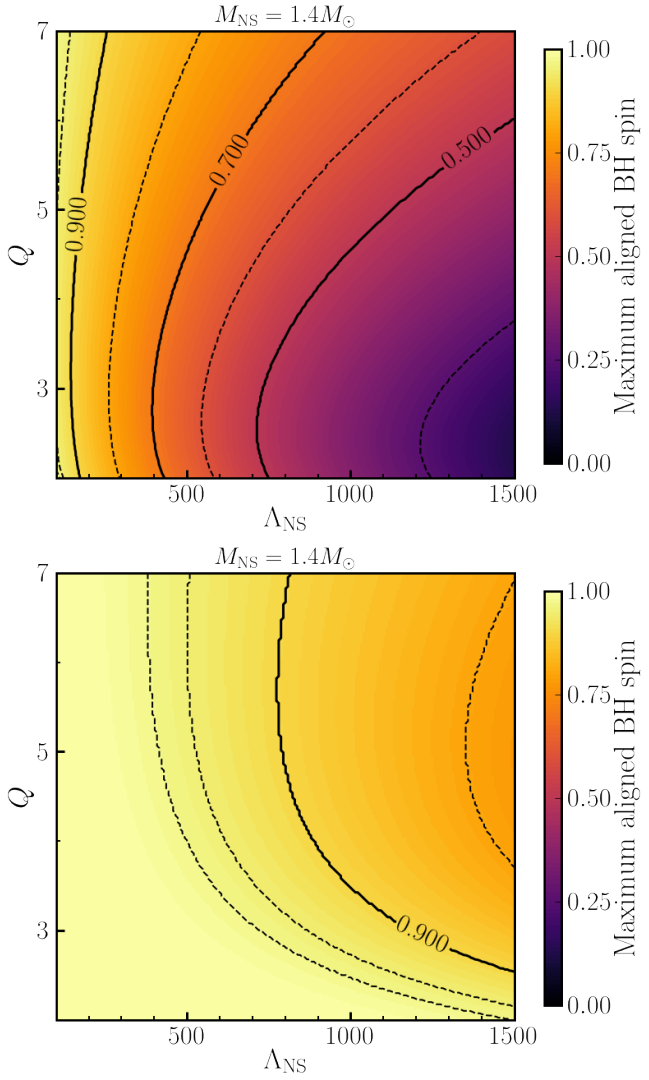

Figure 10. Constraints on the parameter space of black hole-neutron star binaries assuming $M_{ej} < 0.03$ $M_\odot$ (top) and $M_{ej} < 0.1$ $M_\odot$ (bottom). We show the highest possible value of the component of the black hole spin aligned with the orbital momentum as a function of mass ratio $Q = M_{\rm BH}/M_{\rm NS}$ and tidal deformability $\Lambda_{\rm NS}$ of the neutron star. As the analytical models used to generate these constraints are only reliable for spins $a/M^2 \lesssim 0.9$, we see that we can only place reliable constraints for $M_{ej} < 0.03$ $M_\odot$. The figures are obtained assuming $M_{\rm NS} = 1.4M_\odot$, but as the ejected mass is approximately proportional to $M_{\rm NS}$ (at fixed $\Lambda_{\rm NS}$), any choice in the range $M_{\rm NS} \sim (1.2 - 1.6)M_\odot$ would give qualitatively similar constraints.

as a maximum possible value of $\chi_{\rm aligned}$ for each choice of mass ratio and dimensionless neutron star deformability $(Q, \Lambda_{\rm NS})$, as in Fig. 10. The dimensionless neutron star deformability is related to the neutron star EOS, and is given by

$$\Lambda_{\rm NS} = \frac{\lambda c^{10}}{G^4 M_{\rm NS}^5}, \qquad (2)$$

where $\lambda = 2k_2 R_{\rm NS}^5/(3G)$ and k_2 is the so-called "Love number" (see, e.g., Flanagan & Hinderer 2008; Hinderer et al. 2010). Alternatively, we could derive an upper bound on $\Lambda_{\rm NS}$ at fixed $\chi_{\rm aligned}$.

From Figure 10, we see that the conservative bound $M_{\rm ej} < 0.1M_\odot$ does not provide very meaningful constraints on the parameter space of the binary, especially considering that fitting formulae are not properly calibrated above $\chi_{\rm aligned} = 0.9$. With the less certain bound $M_{\rm ej} < 0.03M_\odot$, on the other hand, we can rule out many systems with large neutron stars and/or high (aligned) black hole spins.

Assuming $\Lambda < 800$ (the largest value allowed by GW170817 for a 1.4 $M_\odot$ NS, Abbott et al. 2017) and $M_{ej} < 0.03$ $M_\odot$, the data constrain the BH spin component aligned with the orbital momentum to be $\chi < 0.7$ for mass ratios $Q < 6$. This constraint becomes looser for more compact stars (lower Λ), and tighter for less compact stars (larger Λ).

8. CONCLUSION

In this paper, we have presented deep synoptic limits on the optical counterpart to the NSBH merger S190814bv by analyzing publicly available data from a DECam imaging campaign. We identified dozens of counterpart candidates, and systematically ruled each of them out using the results of a global follow-up campaign undertaken by our group and the community. Real-time data analysis and prompt follow-up allowed the candidates to be classified at timescales from hours to days. Based on our lack of identification of an optical counterpart, we used our detection limits and kilonova models to constrain the allowable parameter space for S190814bv. We found that the ejecta mass can be poorly constrained at the far end of the distance probability distribution, however limits on the ejecta mass of $M_{ej} \lesssim 0.05$ $M_\odot$ can be placed at a luminosity distance of 267 Mpc at polar viewing angles or assuming an opacity $\kappa < 2$ cm^{2}g^{-1}. A more stringent limit of $M_{ej} \lesssim 0.03$ $M_\odot$ can be placed assuming a distance of 215 Mpc. Using the constrains that we obtained for the ejecta mass, we showed how the phase space of the NSBH binary system can also be constrained. In particular, reliable constraints on the highest possible value of the BH spin component aligned with the orbital momentum as a function of Q and Λ_{NS} can be placed for $M_{ej} < 0.03$ $M_\odot$. In that regime, we can constrain the spin component to be $\chi < 0.7$ for mass ratios $Q < 6$. The non-detection of a viable counterpart to S190814bv is also consistent with the progenitor being a low-mass binary BH, rather than a NSBH system.

Follow-up observations of new NSBH mergers with DECam and transient characterization with telescope networks have great potential to unveil electromagnetic counterparts during O3 and beyond. Non-detections such as this one can significantly constrain the parameter space of NSBH merger and kilonova models. In the near future, follow-up campaigns with LSST will allow us to probe NSBH mergers deeper and at larger distances.

ACKNOWLEDGMENTS

This work was supported by the GROWTH (Global Relay of Observatories Watching Transients Happen) project funded by the National Science Foundation under PIRE Grant No 1545949. GROWTH is a collaborative project among California Institute of Technology (USA), University of Maryland College Park (USA), University of Wisconsin Milwaukee (USA), Texas Tech University (USA), San Diego State University (USA), University of Washington (USA), Los Alamos National Laboratory (USA), Tokyo Institute of Technology (Japan), National Central University (Taiwan), Indian Institute of Astrophysics (India), Indian Institute of Technology Bombay (India), Weizmann Institute of Science (Israel), The Oskar Klein Centre at Stockholm University (Sweden), Humboldt University (Germany), Liverpool John Moores University (UK) and University of Sydney (Australia).

Daniel A. Goldstein acknowledges support from Hubble Fellowship grant HST-HF2-51408.001-A. Support for Program number HST-HF2-51408.001-A is provided by NASA through a grant from the Space Telescope Science Institute, which is operated by the Association of Universities for Research in Astronomy, Incorporated, under NASA contract NAS5-26555. We gratefully acknowledge Amazon Web Services, Inc. for a generous grant (`PS_IK_FY2019_Q3_Caltech_Gravitational_Wave`) that funded our use of the Amazon Web Services cloud computing infrastructure to process the DECam data.

P. E. Nugent acknowledges support from the DOE through DE-FOA-0001088, Analytical Modeling for Extreme-Scale Computing Environments. D. A. Perley and D. A. Goldstein performed the work associated with this project at the Aspen Center for Physics which is supported by National Science Foundation grant PHY-1607611. This work was partially supported by a grant from the Simons Foundation. AJCT thanks I. Agudo, J. Cepa, V. Dhillon, J. Cepa, A. Martin-Carrillo, S. R. Oates, S. B. Pandey, E. Pian, R. Sanchez-Ramirez, A. M. Sintes, V. Sokolov and B.-B. Zhang for fruitful conversations. M. Bulla, A. Goobar, E. Kool, S. Dhawan, and J. Sollerman acknowledge support from the G.R.E.A.T research environment funded by the Swedish National Science Foundation. J. Sollerman acknowledges support from the Knut and Alice Wallenberg Foundation. J. S. Bloom and K. Zhang are partially supported by a Gordon and Betty Moore Foundation Data-Driven Discovery grant. D. A. H. Buckley acknowledges research support from the National Research Foundation of South Africa. M. W. Coughlin is supported by the David and Ellen Lee Postdoctoral Fellowship at the California Institute of Technology. S. Nissanke and G. Raaijmakers are grateful for support from VIDI, Projectruimte and TOP Grants of the Innovational Research Incentives Scheme (Vernieuwingsimpuls) financed by the Netherlands Organization for Scientific Research (NWO). H. Kumar and K. Zhang thank the LSSTC Data Science Fellowship Program, which is funded by LSSTC, NSF Cybertraining Grant #1829740, the Brinson Foundation, and the Moore Foundation; his participation in the program has benefited this work. D. Dobie is supported by an Australian Government Research Training Program Scholarship. P. Gatkine is supported by NASA Earth and Space Science Fellowship (ASTRO18F-0085). D. L. Kaplan was supported by NSF grant AST-1816492. Y.D. Hu thanks the support by the program of China Scholarships Council (CSC) under the Grant No.201406660015. A. K. H. Kong acknowledges support from the Ministry of Science and Technology of the Republic of China (Taiwan) through grants 107-2628-M-007-003 and 108-2628-M-007-005-RSP. V. Z. Golkhou acknowledges support from the University of Washington College of Arts and Sciences, Department of Astronomy, and the DIRAC Institute. University of Washington's DIRAC Institute is supported through generous gifts from the Charles and Lisa Simonyi Fund for Arts and Sciences, and the Washington Research Foundation. M. Juric and A. Connolly acknowledge the support of the Washington Research Foundation Data Science Term Chair fund, and the UW Provost's Initiative in Data-Intensive Discovery. S. Mohite thanks the LSSTC Data Science Fellowship Program, which is funded by LSSTC, NSF Cybertraining Grant-1829740, the Brinson Foundation, and the Moore Foundation; his participation in the program has benefited this work. MG is supported by the Polish NCN MAESTRO grant 2014/14/A/ST9/00121.

This research has made use of the VizieR catalogue access tool, CDS, Strasbourg, France (DOI: `10.26093/cds/vizier`). The original description of the VizieR service was published in A&AS 143, 23. This project used data obtained with the Dark Energy Camera (DECam), which was constructed by

the Dark Energy Survey (DES) collaborating institutions: Argonne National Lab, University of California Santa Cruz, University of Cambridge, Centro de Investigaciones Energeticas, Medioambientales y Tecnologicas-Madrid, University of Chicago, University College London, DES-Brazil consortium, University of Edinburgh, ETH-Zurich, University of Illinois at Urbana-Champaign, Institut de Ciencies de l'Espai, Institut de Fisica d'Altes Energies, Lawrence Berkeley National Lab, Ludwig-Maximilians Universitat, University of Michigan, National Optical Astronomy Observatory, University of Nottingham, Ohio State University, University of Pennsylvania, University of Portsmouth, SLAC National Lab, Stanford University, University of Sussex, and Texas A&M University. Funding for DES, including DECam, has been provided by the U.S. Department of Energy, National Science Foundation, Ministry of Education and Science (Spain), Science and Technology Facilities Council (UK), Higher Education Funding Council (England), National Center for Supercomputing Applications, Kavli Institute for Cosmological Physics, Financiadora de Estudos e Projetos, Fundação Carlos Chagas Filho de Amparo a Pesquisa, Conselho Nacional de Desenvolvimento Científico e Tecnológico and the Ministério da Ciência e Tecnologia (Brazil), the German Research Foundation-sponsored cluster of excellence "Origin and Structure of the Universe" and the DES collaborating institutions.

The Liverpool Telescope is operated on the island of La Palma by Liverpool John Moores University in the Spanish Observatorio del Roque de los Muchachos of the Instituto de Astrofisica de Canarias with financial support from the UK Science and Technology Facilities Council. Based on observations made with the Gran Telescopio Canarias (GTC), installed in the Spanish Observatorio del Roque de los Muchachos of the Instituto de Astrofísica de Canarias, in the island of La Palma. This work is partly based on data obtained with the instrument OSIRIS, built by a Consortium led by the Instituto de Astrofísica de Canarias in collaboration with the Instituto de Astronomía of the Universidad Autónoma de México. OSIRIS was funded by GRANTECAN and the National Plan of Astronomy and Astrophysics of the Spanish Government. Some of the observations reported in this paper were obtained with the Southern African Large Telescope (SALT). Polish participation in SALT is funded by grant no. MNiSW DIR/WK/2016/07.

REFERENCES

Abadie, J., Abbott, B. P., Abbott, R., et al. 2010, Classical and Quantum Gravity, 27, 173001

Abbott, B., et al. 2016, Physical Review Letters, 116, 061102

—. 2017, Phys. Rev. Lett., 119, 161101

Abbott, B. P., Abbott, R., Abbott, T. D., et al. 2019, Physical Review X, 9, 031040

Andreoni, I., Goldstein, D. A., Ahumada, T., et al. 2019, GCN, 25362

Annis, J., Herner, K., & Soares-Santos, M. 2019, GCN, 25458

Barbieri, C., Salafia, O. S., Perego, A., Colpi, M., & Ghirlanda, G. 2019, A&A, 625, A152

Becker, A. 2015, HOTPANTS: High Order Transform of PSF ANd Template Subtraction, ascl:1504.004

Belkin, S., Pozanenko, A., Inasaridze, R. Y., et al. 2019, GCN, 25392

Blagorodnova, N., Neill, J. D., Walters, R., et al. 2018, PASP, 130, 035003

Blondin, S., & Tonry, J. L. 2007, ApJ, 666, 1024

Bruun, S. H., Sagues Carracedo, A., Chen, T. W., et al. 2019, GCN, 25384

Buckley, D., Ciroi, S., Gromadzski, M., et al. 2019, GCN, 25481

Buckley, D. A. H., Swart, G. P., & Meiring, J. G. 2006, in Proc. SPIE, Vol. 6267, 62670Z

Buckley, D. A. H., Andreoni, I., Barway, S., et al. 2018, MNRAS, 474, L71

Bulla, M. 2019, MNRAS, 489, 5037

Bulla, M., Covino, S., Kyutoku, K., et al. 2019, Nature Astronomy, 3, 99

Burgh, E. B., Nordsieck, K. H., Kobulnicky, H. A., et al. 2003, in Proc. SPIE, Vol. 4841, Instrument Design and Performance for Optical/Infrared Ground-based Telescopes, ed. M. Iye & A. F. M. Moorwood, 1463–1471

Burrows, D. N., Hill, J. E., Nousek, J. A., et al. 2005, SSRv, 120, 165

Castro-Tirado, A. J., Valeev, A. F., Hu, Y. D., et al. 2019, GCN, 25543

Cepa, J., Aguiar, M., Escalera, V. G., et al. 2000, in Society of Photo-Optical Instrumentation Engineers (SPIE) Conference Series, Vol. 4008, Proc. SPIE, ed. M. Iye & A. F. Moorwood, 623–631

Chambers, K. C., Magnier, E. A., Metcalfe, N., et al. 2016, arXiv e-prints, arXiv:1612.05560

Chen, T. W., Schweyer, T., Nicuesa Guelbenzu, A., et al. 2019, GCN, 25457

Christie, I. M., Lalakos, A., Tchekhovskoy, A., et al. 2019, arXiv:1907.02079

Colless, M., Dalton, G., Maddox, S., et al. 2001, MNRAS, 328, 1039

Corre, D., Blazek, M., Klotz, A., et al. 2019, GCN, 25599

Corwin, Jr., H. G., Buta, R. J., & de Vaucouleurs, G. 1994, AJ, 108, 2128

Coughlin, M., Ahumada, T., & Anand, S. 2019, GCN, 25477

Coulter, D. A., Foley, R. J., Kilpatrick, C. D., et al. 2017, Science, 358, 1556

Cowperthwaite, P. S., Berger, E., Villar, V. A., et al. 2017, ApJ, 848, L17

Crawford, S. M., Still, M., Schellart, P., et al. 2010, in Proc. SPIE, Vol. 7737, Observatory Operations: Strategies, Processes, and Systems III, 773725

Cushing, M. C., Vacca, W. D., & Rayner, J. T. 2004, PASP, 116, 362

Dálya, G., Galgóczi, G., Dobos, L., et al. 2018, MNRAS, 479, 2374

Dark Energy Survey Collaboration, Abbott, T., Abdalla, F. B., et al. 2016, MNRAS, 460, 1270

D'Avanzo, P., Giunta, A., Izzo, L., et al. 2019, GCN, 25401

De, K., Goldstein, D., Andreoni, I., et al. 2019a, GCN, 25348

De, K., Jencson, J., Kasliwal, M. M., Goldstein, D., & Andreoni, I. 2019b, GCN, 25478

De, K., Kasliwal, M. M., Andreoni, I., Karambelkar, V., & Sharma, Y. 2019c, GCN, 25461

De, K., Tinyanont, S., Kamraj, N., et al. 2019d, GCN, 25396

de Vaucouleurs, G., de Vaucouleurs, A., Corwin, Jr., H. G., et al. 1991, Third Reference Catalogue of Bright Galaxies. Volume I: Explanations and references. Volume II: Data for galaxies between 0^h and 12^h. Volume III: Data for galaxies between 12^h and 24^h.

Dey, A., Schlegel, D. J., Lang, D., et al. 2019, AJ, 157, 168

Dhawan, S., Bulla, M., Goobar, A., Sagués Carracedo, A., & Setzer, C. N. 2019, arXiv e-prints, arXiv:1909.13810

Dichiara, S., Troja, E., Watson, A. M., et al. 2019a, GCN, 25416

Dichiara, S., Troja, E., Cenko, S. B., et al. 2019b, GCN, 25374

—. 2019c, GCN, 25397

Dobie, D., Murphy, T., Lenc, E., et al. 2019, GCN, 25472

Drout, M. R., Piro, A. L., Shappee, B. J., et al. 2017, Science, 358, 1570

Evans, P. A., Kennea, J. A., Tohuvavohu, A., et al. 2019, GCN, 25400

Fernández, R., Foucart, F., Kasen, D., et al. 2017, Classical and Quantum Gravity, 34, 154001

Fernandez, R., & Metzger, B. D. 2013, Mon. Not. Roy. Astron. Soc., 435, 502

Fernández, R., & Metzger, B. D. 2016, Annual Review of Nuclear and Particle Science, 66, 23

Fernández, R., Kasen, D., Metzger, B. D., & Quataert, E. 2015, Mon. Not. Roy. Astron. Soc., 446, 750

Flanagan, É. É., & Hinderer, T. 2008, prd, 77, 021502

Flaugher, B., Diehl, H. T., Honscheid, K., et al. 2015, AJ, 150, 150

Foucart, F. 2012, Phys. Rev., D86, 124007

Foucart, F., Hinderer, T., & Nissanke, S. 2018, Phys. Rev., D98, 081501

Fremling, C., Goldstein, D., Andreoni, I., & Kasliwal, M. M. 2019, GCN, 25460

Fremling, C., Sollerman, J., Taddia, F., et al. 2016, A&A, 593, A68

Geesaman, D. 2015, in APS Meeting Abstracts, AA1.001

Gehrels, N., Cannizzo, J. K., Kanner, J., et al. 2016, ApJ, 820, 136

Goldstein, D. A., & Anand, S. 2019, GCN, 25393

Goldstein, D. A., Perley, D., Andreoni, I., & Kasliwal, M. M. 2019, GCN, 25355

Goldstein, D. A., D'Andrea, C. B., Fischer, J. A., et al. 2015, AJ, 150, 82

Goldstein, D. A., Andreoni, I., Nugent, P. E., et al. 2019, ApJ, 881, L7

Goldstein, D. A., Andreoni, I., Hankins, M., et al. 2019a, GCN, 25393

Goldstein, D. A., Andreoni, I., Zhou, R., et al. 2019b, GCN, 25391

Gomez, S., Hosseinzadeh, G., Cowperthwaite, P. S., et al. 2019, arXiv e-prints, arXiv:1908.08913

Gomez, S., Hosseinzadeh, G., Berger, E., et al. 2019, GCN, 25483

Greggio, L., Rejkuba, M., Gonzalez, O. A., et al. 2014, A&A, 562, A73

Herner, K., Palmese, A., Soares-Santos, M., et al. 2019a, GCN, 25398

—. 2019b, GCN, 25373

Hinderer, T., Lackey, B. D., Lang, R. N., & Read, J. S. 2010, prd, 81, 123016

Hotokezaka, K., & Nakar, E. 2019, arXiv e-prints, arXiv:1909.02581

Hu, Y. D., Castro-Tirado, A. J., Valeev, A. F., et al. 2019, GCN, 25588

Huber, M., Smith, K. W., Chambers, K., et al. 2019, GCN, 25356

Jonker, P., Maguire, K., Fraser, M., et al. 2019, GCN, 25454

Kasliwal, M. M., Nakar, E., Singer, L. P., et al. 2017, Science, 358, 1559

Kasliwal, M. M., Cannella, C., Bagdasaryan, A., et al. 2019, PASP, 131, 038003

Kawaguchi, K., Kyutoku, K., Shibata, M., & Tanaka, M. 2016, Astrophys. J., 825, 52

Kilpatrick, C. D., Foley, R. J., Kasen, D., et al. 2017, Science, 358, 1583

Kobulnicky, H. A., Nordsieck, K. H., Burgh, E. B., et al. 2003, in Society of Photo-Optical Instrumentation Engineers (SPIE) Conference Series, Vol. 4841, Proc. SPIE, ed. M. Iye & A. F. M. Moorwood, 1634–1644

Lattimer, J. M., & Schramm, D. N. 1974, ApJ, 192, L145

LIGO Scientific Collaboration, & Virgo Collaboration. 2019, GCN, 24448

Lipunov, V., Vlasenko, D., Gorbovskoy, E., et al. 2019, GCN, 25474

Lopez-Cruz, O., Castro-Tirado, A. J., Macri, L., et al. 2019a, GCN, 25571

—. 2019b, GCN, 25419

Luri, X., Brown, A. G. A., Sarro, L. M., et al. 2018, A&A, 616, A9

McBrien, O. R., Srivastav, S., Smith, K. W., et al. 2019, GCN, 25346

Metzger, B. D., & Berger, E. 2012, ApJ, 746, 48

Mingarelli, C. M. F., Levin, J., & Lazio, T. J. W. 2015, ApJ, 814, L20

Mooley, K., Hallinan, G., Kasliwal, M. M., Corsi, A., & Frail, D. 2019, GCN, 25480

Nissanke, S., Kasliwal, M., & Georgieva, A. 2013, ApJ, 767, 124

Nordin, J., Brinnel, V., Giomi, M., et al. 2019, Transient Name Server Discovery Report, 2019-1370, 1

Oke, J. B., Cohen, J. G., Carr, M., et al. 1995, PASP, 107, 375

Özel, F., & Freire, P. 2016, ARA&A, 54, 401

Palmese, A., Annis, J., & Soares-Santos, M. 2019, GCN, 25468

Perley, D. A. 2019, PASP, 131, 084503

Rodríguez, O., Meza-Retamal, N., Quirola, J., et al. 2019, GCN, 25423

Schutz, B. F. 1986, Nature, 323, 310

Siegel, D. M., & Metzger, B. D. 2017, Phys. Rev. Lett., 119, 231102

Singer, L. P., Chen, H.-Y., Holz, D. E., et al. 2016, ApJ, 829, L15

Smartt, S., Smith, K. W., Srivastav, S., et al. 2019, GCN, 25455

Soares-Santos, M., Tucker, D., Allam, S., et al. 2019a, GCN, 25336

Soares-Santos, M., Annis, J., Herner, K., et al. 2019b, GCN, 25486

Soares-Santos, M., Annis, J., Garcia, A., et al. 2019c, GCN, 25425

—. 2019d, GCN, 25438

Steele, I. A., Smith, R. J., Rees, P. C., et al. 2004, in Society of Photo-Optical Instrumentation Engineers (SPIE) Conference Series, Vol. 5489, Proc. SPIE, ed. J. Oschmann, Jacobus M., 679–692

Tanaka, M., Kato, D., Gaigalas, G., et al. 2018, ApJ, 852, 109

The LIGO Scientific Collaboration, & The Virgo Collaboration. 2019a, GRB Coordinates Network, 24228, 1

—. 2019b, GRB Coordinates Network, 24277, 1

The LIGO Scientific Collaboration and the Virgo Collaboration. 2019a, GCN, 25324

—. 2019b, GCN, 25333

Tucker, D., Allam, S., Wiesner, M., et al. 2019a, GCN, 25379

Tucker, D., Butner, M., Wiesner, M., et al. 2019b, GCN, 25484

Veitch, J., Raymond, V., Farr, B., et al. 2015, Phys. Rev. D, 91, 042003

Wang, X., Antier, S., Coughlin, M., et al. 2019, GCN, 25485

Wiesner, M., Butner, M., Allam, S., et al. 2019a, GCN, 25596

Wiesner, M., Butner, M., Tucker, D., et al. 2019b, GCN, 25540

Wilson, J. C., Eikenberry, S. S., Henderson, C. P., et al. 2003, in Society of Photo-Optical Instrumentation Engineers (SPIE) Conference Series, Vol. 4841, Proc. SPIE, ed. M. Iye & A. F. M. Moorwood, 451–458

Wright, E. L., Eisenhardt, P. R. M., Mainzer, A. K., et al. 2010, AJ, 140, 1868

Yang, S., Cappellaro, E., Grado, A., et al. 2019, GCN, 25748

APPENDIX

Table 5. DECam photometry of candidates listed in Tables 2 and 3.

Internal Name	MJD	Filter	m	σ_m	$m_{\rm lim}$
DG19aferc	58710.294884	i	···	···	21.15
DG19aferc	58710.295921	z	···	···	21.30
DG19aferc	58711.250669	i	···	···	21.12
DG19aferc	58711.267294	i	···	···	20.98
DG19aferc	58711.327283	i	···	···	21.88
DG19aferc	58711.359925	i	···	···	21.87
DG19aferc	58712.240520	i	···	···	22.05
DG19aferc	58712.242019	z	···	···	22.65
DG19aferc	58712.299779	i	···	···	21.92
DG19aferc	58712.316480	i	···	···	22.20
DG19aferc	58712.377441	i	···	···	21.90
DG19aferc	58712.378929	z	···	···	21.52
DG19aferc	58713.266558	i	22.12	0.14	22.63
DG19aferc	58713.283160	i	22.34	0.14	22.86
DG19aferc	58713.348863	i	···	···	22.69
DG19aferc	58713.370145	i	22.15	0.13	22.75
DG19aferc	58716.196156	i	22.46	0.09	23.52
DG19aferc	58716.217530	i	21.99	0.07	23.35
DG19aferc	58716.260514	i	22.41	0.12	23.04
DG19aferc	58716.281851	i	22.42	0.11	23.18
DG19aferc	58726.197980	i	22.43	0.06	23.99
DG19aferc	58726.239776	i	22.24	0.06	24.11
DG19bown	58710.275153	i	···	···	20.61
DG19bown	58710.280991	z	···	···	21.07
DG19bown	58710.282368	i	···	···	21.31
DG19bown	58710.283386	z	···	···	20.27
DG19bown	58710.327043	i	···	···	20.20
DG19bown	58710.332884	z	···	···	19.97
DG19bown	58710.334265	i	···	···	20.23
DG19bown	58710.335291	z	···	···	20.38
DG19bown	58711.231432	z	···	···	21.71
DG19bown	58711.234090	i	···	···	21.18
DG19bown	58711.243856	z	···	···	21.22
DG19bown	58711.310105	i	···	···	21.81
DG19bown	58711.320161	z	···	···	22.15
DG19bown	58712.204660	z	···	···	22.03
DG19bown	58712.207300	i	···	···	21.90
DG19bown	58712.217093	z	···	···	22.17
DG19bown	58712.280436	z	···	···	22.11
DG19bown	58712.283084	i	···	···	22.00
DG19bown	58712.292874	z	···	···	22.01
DG19bown	58712.358145	z	···	···	22.34

Table 5 continued

Table 5 *(continued)*

Internal Name	MJD	Filter	m	σ_m	$m_{\rm lim}$
DG19bown	58712.360780	i	···	···	22.01
DG19bown	58712.370635	z	22.16	0.19	22.29
DG19bown	58713.247322	z	···	···	22.67
DG19bown	58713.249972	i	···	···	22.30
DG19bown	58713.259765	z	···	···	22.76
DG19bown	58713.324292	z	22.72	0.20	22.84
DG19bown	58713.327524	i	···	···	22.77
DG19bown	58713.340233	z	···	···	22.78
DG19bown	58716.171752	z	22.90	0.14	23.43
DG19bown	58716.174965	i	22.94	0.13	23.56
DG19bown	58716.187630	z	23.00	0.14	23.52
DG19bown	58716.236111	z	22.88	0.19	23.07
DG19bown	58716.239337	i	22.89	0.17	23.18
DG19bown	58716.251989	z	22.74	0.17	22.99
DG19bown	58716.300714	z	···	···	22.65
DG19bown	58716.303928	i	22.68	0.18	22.89
DG19bown	58716.316802	z	···	···	22.73
DG19bown	58726.200897	i	23.24	0.11	24.02
DG19bown	58726.221691	i	23.12	0.09	24.22
DG19bown	58726.242668	i	23.14	0.08	24.28
DG19bpkf	58711.267294	i	···	···	20.92
DG19bpkf	58711.268777	z	···	···	21.04
DG19bpkf	58711.345896	z	···	···	21.85
DG19bpkf	58711.359925	i	···	···	21.82
DG19bpkf	58712.240520	i	···	···	22.00
DG19bpkf	58712.242019	z	···	···	22.07
DG19bpkf	58712.316480	i	···	···	22.15
DG19bpkf	58712.317973	z	···	···	22.56
DG19bpkf	58713.283160	i	···	···	22.85
DG19bpkf	58713.284657	z	···	···	22.96
DG19bpkf	58713.370145	i	22.82	0.21	22.87
DG19bpkf	58713.372217	z	···	···	22.51
DG19bpkf	58716.217530	i	···	···	23.31
DG19bpkf	58716.219595	z	···	···	23.24
DG19bpkf	58716.281851	i	···	···	23.22
DG19bpkf	58716.283904	z	···	···	23.04
DG19bpkf	58726.197980	i	23.22	0.11	24.06
DG19bpkf	58726.218800	i	23.41	0.10	24.29
DG19bpkf	58726.239776	i	23.70	0.14	24.18
DG19fcmgc	58710.272724	i	18.75	0.04	21.33
DG19fcmgc	58710.273768	z	18.58	0.03	21.01
DG19fcmgc	58711.229951	i	18.72	0.04	20.87
DG19fcmgc	58711.305961	i	18.78	0.03	21.67
DG19fcmgc	58712.278943	i	18.75	0.03	22.25
DG19fcmgc	58712.356658	i	18.75	0.03	22.10
DG19fcmgc	58713.245809	i	18.80	0.02	22.40
DG19fcmgc	58713.322221	i	18.73	0.03	22.80

Table 5 continued

Table 5 *(continued)*

Internal Name	MJD	Filter	m	σ_m	$m_{\rm lim}$
DG19fcmgc	58716.169683	i	18.79	0.03	23.48
DG19fcmgc	58716.234025	i	18.79	0.03	23.26
DG19fcmgc	58716.298638	i	18.78	0.03	22.71
DG19ggesc	58710.279955	i	···	···	20.69
DG19ggesc	58710.280991	z	···	···	21.09
DG19ggesc	58710.332884	z	···	···	19.94
DG19ggesc	58711.231432	z	···	···	21.73
DG19ggesc	58711.242363	i	···	···	21.20
DG19ggesc	58711.243856	z	···	···	21.24
DG19ggesc	58711.318679	i	···	···	22.11
DG19ggesc	58711.320161	z	···	···	22.16
DG19ggesc	58712.204660	z	21.32	0.12	21.99
DG19ggesc	58712.215600	i	···	···	21.92
DG19ggesc	58712.217093	z	21.81	0.15	22.20
DG19ggesc	58712.280436	z	···	···	22.10
DG19ggesc	58712.291373	i	···	···	22.27
DG19ggesc	58712.292874	z	21.97	0.20	22.04
DG19ggesc	58712.358145	z	···	···	22.34
DG19ggesc	58712.369148	i	···	···	22.31
DG19ggesc	58712.370635	z	···	···	22.32
DG19ggesc	58713.247322	z	···	···	22.65
DG19ggesc	58713.258267	i	···	···	22.59
DG19ggesc	58713.259765	z	22.67	0.20	22.76
DG19ggesc	58713.324292	z	22.76	0.20	22.85
DG19ggesc	58713.338159	i	···	···	22.79
DG19ggesc	58713.340233	z	22.34	0.15	22.77
DG19ggesc	58716.171752	z	22.58	0.10	23.41
DG19ggesc	58716.185565	i	23.15	0.15	23.60
DG19ggesc	58716.187630	z	22.60	0.10	23.47
DG19ggesc	58716.236111	z	22.69	0.15	23.07
DG19ggesc	58716.249927	i	22.74	0.14	23.24
DG19ggesc	58716.251989	z	22.72	0.17	22.99
DG19ggesc	58716.300714	z	···	···	22.60
DG19ggesc	58716.314735	i	22.55	0.19	22.76
DG19ggesc	58716.316802	z	···	···	22.68
DG19ggesc	58726.200897	i	22.79	0.09	23.95
DG19ggesc	58726.203772	i	23.10	0.13	23.71
DG19ggesc	58726.221691	i	23.00	0.09	24.13
DG19ggesc	58726.224569	i	23.07	0.08	24.23
DG19ggesc	58726.242668	i	22.89	0.08	24.18
DG19ggesc	58726.245540	i	23.06	0.10	24.07
DG19gxuqc	58710.282368	i	···	···	21.08
DG19gxuqc	58710.283386	z	···	···	20.33
DG19gxuqc	58710.334265	i	···	···	20.42
DG19gxuqc	58710.335291	z	···	···	20.39
DG19gxuqc	58711.246513	i	···	···	21.21
DG19gxuqc	58711.247990	z	···	···	21.73

Table 5 continued

Table 5 *(continued)*

Internal Name	MJD	Filter	m	σ_m	$m_{\rm lim}$
DG19gxuqc	58711.323118	i	···	···	22.05
DG19gxuqc	58711.324621	z	···	···	22.24
DG19gxuqc	58712.219736	i	···	···	21.96
DG19gxuqc	58712.221236	z	···	···	22.00
DG19gxuqc	58712.295533	i	···	···	22.02
DG19gxuqc	58712.297123	z	···	···	22.18
DG19gxuqc	58712.373291	i	···	···	22.24
DG19gxuqc	58713.262414	i	···	···	22.65
DG19gxuqc	58713.263892	z	22.64	0.19	22.80
DG19gxuqc	58713.343452	i	···	···	22.78
DG19gxuqc	58713.345519	z	22.39	0.16	22.72
DG19gxuqc	58716.190860	i	22.55	0.09	23.70
DG19gxuqc	58716.192927	z	22.81	0.11	23.52
DG19gxuqc	58716.255204	i	22.43	0.10	23.34
DG19gxuqc	58716.257275	z	···	···	22.92
DG19gxuqc	58716.320040	i	22.39	0.15	22.84
DG19gxuqc	58716.322111	z	···	···	22.59
DG19gyvx	58710.292479	i	···	···	21.06
DG19gyvx	58710.293513	z	···	···	20.98
DG19gyvx	58711.238232	i	···	···	21.43
DG19gyvx	58711.239722	z	···	···	21.73
DG19gyvx	58711.314532	i	···	···	21.88
DG19gyvx	58711.316028	z	22.27	0.21	22.30
DG19gyvx	58712.211452	i	···	···	22.07
DG19gyvx	58712.212956	z	···	···	22.09
DG19gyvx	58712.287228	i	···	···	22.16
DG19gyvx	58712.288735	z	···	···	22.07
DG19gyvx	58712.365007	i	···	···	22.29
DG19gyvx	58712.366493	z	···	···	22.46
DG19gyvx	58713.254130	i	···	···	22.57
DG19gyvx	58713.255616	z	22.65	0.20	22.76
DG19gyvx	58713.332843	i	···	···	22.69
DG19gyvx	58713.334931	z	···	···	22.60
DG19gyvx	58716.180267	i	···	···	23.65
DG19gyvx	58716.182342	z	22.75	0.11	23.54
DG19gyvx	58716.244655	i	22.69	0.17	23.30
DG19gyvx	58716.246714	z	22.79	0.16	23.13
DG19gyvx	58716.309431	i	···	···	23.11
DG19gyvx	58716.311507	z	22.47	0.16	22.84
DG19hcsgc	58710.276173	z	20.50	0.12	21.14
DG19hcsgc	58711.229951	i	···	···	21.07
DG19hcsgc	58711.231432	z	20.38	0.07	21.71
DG19hcsgc	58711.235569	z	20.32	0.09	21.38
DG19hcsgc	58711.305961	i	20.43	0.08	21.56
DG19hcsgc	58711.311879	z	20.42	0.05	22.13
DG19hcsgc	58712.203159	i	···	···	12.23
DG19hcsgc	58712.204660	z	20.31	0.05	22.03

Table 5 continued

Table 5 *(continued)*

Internal Name	MJD	Filter	m	σ_m	$m_{\rm lim}$
DG19hcsgc	58712.208802	z	20.62	0.06	22.06
DG19hcsgc	58712.278943	i	20.27	0.03	22.38
DG19hcsgc	58712.280436	z	20.61	0.06	22.08
DG19hcsgc	58712.284576	z	20.53	0.05	22.19
DG19hcsgc	58712.356658	i	20.46	0.05	22.09
DG19hcsgc	58712.358145	z	20.47	0.04	22.38
DG19hcsgc	58712.362257	z	20.36	0.04	22.31
DG19hcsgc	58713.245809	i	20.44	0.04	22.33
DG19hcsgc	58713.247322	z	20.39	0.03	22.69
DG19hcsgc	58713.251477	z	20.44	0.04	22.61
DG19hcsgc	58713.322221	i	20.20	0.03	22.69
DG19hcsgc	58713.324292	z	20.47	0.03	22.90
DG19hcsgc	58713.329599	z	20.44	0.04	22.78
DG19hcsgc	58716.169683	i	20.50	0.02	23.53
DG19hcsgc	58716.171752	z	20.68	0.03	23.47
DG19hcsgc	58716.177031	z	20.66	0.04	23.47
DG19hcsgc	58716.234025	i	20.59	0.02	23.31
DG19hcsgc	58716.236111	z	20.55	0.03	23.10
DG19hcsgc	58716.241409	z	20.53	0.03	23.04
DG19hcsgc	58716.298638	i	20.50	0.03	22.81
DG19hcsgc	58716.300714	z	20.51	0.04	22.64
DG19hcsgc	58716.306173	z	20.50	0.04	22.76
DG19hcsgc	58726.200897	i	20.56	0.02	23.93
DG19hcsgc	58726.221691	i	20.61	0.02	24.10
DG19hcsgc	58726.242668	i	20.57	0.02	24.18
DG19hqhjc	58710.277547	i	···	···	21.17
DG19hqhjc	58710.278567	z	···	···	20.76
DG19hqhjc	58711.235569	z	···	···	21.38
DG19hqhjc	58711.263132	i	···	···	20.69
DG19hqhjc	58711.310105	i	···	···	21.84
DG19hqhjc	58711.311879	z	21.95	0.20	22.13
DG19hqhjc	58711.340265	i	···	···	21.45
DG19hqhjc	58712.283084	i	21.10	0.09	22.12
DG19hqhjc	58712.312326	i	···	···	22.36
DG19hqhjc	58712.360780	i	21.41	0.13	22.04
DG19hqhjc	58712.362257	z	21.99	0.17	22.40
DG19hqhjc	58713.249972	i	21.89	0.14	22.36
DG19hqhjc	58713.251477	z	21.99	0.14	22.68
DG19hqhjc	58713.279009	i	22.21	0.14	22.74
DG19hqhjc	58713.327524	i	21.90	0.10	22.82
DG19hqhjc	58713.329599	z	22.02	0.13	22.82
DG19hqhjc	58713.364773	i	22.14	0.13	22.69
DG19hqhjc	58716.174965	i	21.97	0.06	23.64
DG19hqhjc	58716.177031	z	21.97	0.09	23.50
DG19hqhjc	58716.212200	i	22.13	0.08	23.37
DG19hqhjc	58716.239337	i	22.20	0.09	23.20
DG19hqhjc	58716.241409	z	21.95	0.11	23.07

Table 5 continued

Table 5 *(continued)*

Internal Name	MJD	Filter	m	σ_m	$m_{\rm lim}$
DG19hqhjc	58716.276562	i	···	···	22.97
DG19hqhjc	58716.303928	i	21.85	0.07	23.08
DG19hqhjc	58716.306173	z	22.11	0.13	22.88
DG19hqhjc	58726.209543	i	21.96	0.04	24.03
DG19hqhjc	58726.230348	i	21.83	0.03	24.16
DG19hqhjc	58726.251423	i	21.92	0.03	24.30
DG19ilqnc	58710.292479	i	···	···	21.09
DG19ilqnc	58710.293513	z	···	···	21.07
DG19ilqnc	58711.238232	i	···	···	21.29
DG19ilqnc	58711.314532	i	···	···	21.77
DG19ilqnc	58712.211452	i	···	···	21.97
DG19ilqnc	58712.287228	i	···	···	22.08
DG19ilqnc	58712.365007	i	···	···	22.18
DG19ilqnc	58713.254130	i	22.12	0.17	22.46
DG19ilqnc	58713.332843	i	21.99	0.14	22.53
DG19ilqnc	58716.180267	i	22.28	0.08	23.55
DG19ilqnc	58716.244655	i	22.55	0.13	23.17
DG19ilqnc	58716.309431	i	22.47	0.15	22.95
DG19kpykc	58710.285939	z	···	···	20.03
DG19kpykc	58711.250669	i	···	···	21.18
DG19kpykc	58711.252151	z	···	···	21.33
DG19kpykc	58711.327283	i	21.48	0.15	21.92
DG19kpykc	58711.328771	z	···	···	21.72
DG19kpykc	58712.377441	i	···	···	22.02
DG19kpykc	58712.378929	z	21.92	0.18	22.11
DG19kpykc	58713.266558	i	21.64	0.10	22.67
DG19kpykc	58713.348863	i	21.65	0.09	22.73
DG19kpykc	58716.196156	i	21.55	0.06	23.62
DG19kpykc	58716.198218	z	21.63	0.05	23.37
DG19kpykc	58716.260514	i	21.25	0.06	23.11
DG19lkunc	58711.246513	i	···	···	21.20
DG19lkunc	58711.247990	z	···	···	21.76
DG19lkunc	58711.323118	i	21.77	0.17	22.06
DG19lkunc	58711.324621	z	21.95	0.17	22.26
DG19lkunc	58712.219736	i	···	···	21.94
DG19lkunc	58712.221236	z	···	···	21.99
DG19lkunc	58712.295533	i	···	···	22.00
DG19lkunc	58712.297123	z	21.99	0.18	22.21
DG19lkunc	58712.373291	i	21.72	0.14	22.17
DG19lkunc	58712.374788	z	22.20	0.21	22.25
DG19lkunc	58713.262414	i	21.72	0.10	22.62
DG19lkunc	58713.263892	z	22.01	0.11	22.80
DG19lkunc	58713.343452	i	21.90	0.11	22.70
DG19lkunc	58713.345519	z	22.01	0.12	22.68
DG19lkunc	58716.190860	i	21.88	0.05	23.70
DG19lkunc	58716.192927	z	22.11	0.07	23.52
DG19lkunc	58716.255204	i	22.02	0.07	23.32

Table 5 continued

Table 5 *(continued)*

Internal Name	MJD	Filter	m	σ_m	$m_{\rm lim}$
DG19lkunc	58716.257275	z	22.17	0.12	22.91
DG19lkunc	58716.320040	i	22.01	0.09	22.93
DG19lkunc	58716.322111	z	22.06	0.13	22.65
DG19lsugc	58710.279955	i	20.10	0.14	20.64
DG19lsugc	58710.280991	z	20.06	0.10	21.06
DG19lsugc	58710.332884	z	...	...	19.95
DG19lsugc	58711.229951	i	20.10	0.12	20.83
DG19lsugc	58711.231432	z	20.26	0.07	21.74
DG19lsugc	58711.242363	i	20.09	0.10	21.19
DG19lsugc	58711.243856	z	20.29	0.10	21.25
DG19lsugc	58711.305961	i	19.87	0.06	21.69
DG19lsugc	58711.318679	i	20.05	0.08	22.09
DG19lsugc	58711.320161	z	20.20	0.06	22.15
DG19lsugc	58712.203159	i	19.97	0.06	21.66
DG19lsugc	58712.204660	z	20.13	0.05	22.03
DG19lsugc	58712.215600	i	20.06	0.08	21.90
DG19lsugc	58712.217093	z	20.15	0.05	22.19
DG19lsugc	58712.278943	i	20.06	0.06	22.19
DG19lsugc	58712.280436	z	20.01	0.05	22.10
DG19lsugc	58712.291373	i	20.12	0.07	22.26
DG19lsugc	58712.292874	z	20.19	0.06	22.04
DG19lsugc	58712.356658	i	20.11	0.06	22.12
DG19lsugc	58712.358145	z	20.08	0.06	22.34
DG19lsugc	58712.369148	i	20.07	0.07	22.28
DG19lsugc	58712.370635	z	20.13	0.06	22.30
DG19lsugc	58713.245809	i	20.07	0.05	22.38
DG19lsugc	58713.247322	z	20.14	0.04	22.67
DG19lsugc	58713.258267	i	20.03	0.07	22.57
DG19lsugc	58713.259765	z	20.11	0.05	22.77
DG19lsugc	58713.322221	i	20.13	0.05	22.73
DG19lsugc	58713.324292	z	20.14	0.04	22.87
DG19lsugc	58713.338159	i	20.01	0.08	22.77
DG19lsugc	58713.340233	z	20.18	0.05	22.75
DG19lsugc	58716.169683	i	20.06	0.06	23.44
DG19lsugc	58716.171752	z	20.14	0.06	23.42
DG19lsugc	58716.185565	i	20.04	0.07	23.59
DG19lsugc	58716.187630	z	20.14	0.05	23.54
DG19lsugc	58716.234025	i	20.10	0.05	23.23
DG19lsugc	58716.236111	z	20.15	0.04	23.10
DG19lsugc	58716.249927	i	20.05	0.07	23.25
DG19lsugc	58716.251989	z	20.15	0.05	23.01
DG19lsugc	58716.298638	i	20.09	0.05	22.86
DG19lsugc	58716.300714	z	20.11	0.05	22.60
DG19lsugc	58716.314735	i	20.06	0.07	22.76
DG19lsugc	58716.316802	z	20.13	0.05	22.71
DG19lsugc	58726.200897	i	20.14	0.04	23.99
DG19lsugc	58726.203772	i	20.12	0.05	23.78

Table 5 continued

Table 5 *(continued)*

Internal Name	MJD	Filter	m	σ_m	$m_{\rm lim}$
DG19lsugc	58726.221691	i	20.13	0.05	24.19
DG19lsugc	58726.242668	i	20.13	0.05	24.25
DG19lsugc	58726.245540	i	20.13	0.06	24.16
DG19qabkc	58710.300130	i	···	···	20.92
DG19qabkc	58710.301157	z	···	···	20.73
DG19qabkc	58711.271643	i	20.80	0.21	20.88
DG19qabkc	58711.273138	z	···	···	21.28
DG19qabkc	58711.284887	i	21.06	0.15	21.52
DG19qabkc	58711.286381	z	21.39	0.12	22.09
DG19qabkc	58711.349874	i	21.12	0.07	22.42
DG19qabkc	58711.351370	z	21.41	0.08	22.56
DG19qabkc	58711.366236	i	21.21	0.09	22.28
DG19qabkc	58711.367725	z	21.34	0.07	22.57
DG19qabkc	58712.244885	i	21.23	0.12	21.98
DG19qabkc	58712.246380	z	21.19	0.09	22.20
DG19qabkc	58712.321148	i	21.27	0.08	22.53
DG19qabkc	58712.322653	z	21.34	0.09	22.32
DG19qabkc	58712.334202	i	21.32	0.08	22.47
DG19qabkc	58712.335699	z	21.42	0.08	22.50
DG19qabkc	58713.287530	i	21.14	0.06	22.82
DG19qabkc	58713.289030	z	21.30	0.05	22.97
DG19qabkc	58713.300476	i	21.13	0.06	22.77
DG19qabkc	58713.301967	z	21.26	0.06	22.84
DG19qabkc	58713.375723	i	21.23	0.06	22.91
DG19qabkc	58713.377790	z	21.28	0.06	22.75
DG19qabkc	58716.223045	i	21.24	0.05	23.42
DG19qabkc	58716.225144	z	21.35	0.05	23.11
DG19qabkc	58716.287509	i	21.25	0.05	23.43
DG19qabkc	58716.289575	z	21.34	0.05	22.98
DG19rzhoc	58711.247990	z	···	···	21.70
DG19rzhoc	58711.263132	i	···	···	20.67
DG19rzhoc	58711.324621	z	···	···	22.17
DG19rzhoc	58711.340265	i	···	···	21.54
DG19rzhoc	58712.221236	z	···	···	21.95
DG19rzhoc	58712.297123	z	21.81	0.16	22.18
DG19rzhoc	58712.312326	i	22.15	0.18	22.37
DG19rzhoc	58712.374788	z	22.10	0.20	22.19
DG19rzhoc	58713.263892	z	22.04	0.12	22.73
DG19rzhoc	58713.279009	i	21.99	0.11	22.74
DG19rzhoc	58713.345519	z	22.02	0.12	22.69
DG19rzhoc	58713.364773	i	21.72	0.10	22.62
DG19rzhoc	58716.192927	z	21.79	0.05	23.43
DG19rzhoc	58716.212200	i	21.55	0.05	23.43
DG19rzhoc	58716.257275	z	21.60	0.07	22.85
DG19rzhoc	58716.276562	i	21.65	0.07	22.95
DG19rzhoc	58716.322111	z	21.64	0.10	22.54
DG19tedsc	58710.284914	i	···	···	20.35

Table 5 continued

Table 5 *(continued)*

Internal Name	MJD	Filter	m	σ_m	$m_{\rm lim}$
DG19tedsc	58710.285939	z	···	···	20.05
DG19tedsc	58710.293513	z	···	···	21.07
DG19tedsc	58711.238232	i	···	···	21.42
DG19tedsc	58711.314532	i	···	···	21.90
DG19tedsc	58712.211452	i	···	···	22.07
DG19tedsc	58712.287228	i	···	···	22.13
DG19tedsc	58712.365007	i	···	···	22.24
DG19tedsc	58713.254130	i	···	···	22.54
DG19tedsc	58713.332843	i	···	···	22.63
DG19tedsc	58716.180267	i	22.70	0.16	23.64
DG19tedsc	58716.244655	i	22.68	0.19	23.30
DG19tedsc	58716.309431	i	22.47	0.18	23.13
DG19wgmjc	58710.294884	i	···	···	21.17
DG19wgmjc	58711.252151	z	···	···	21.25
DG19wgmjc	58711.267294	i	···	···	20.89
DG19wgmjc	58711.318679	i	21.31	0.11	22.14
DG19wgmjc	58711.328771	z	21.57	0.18	21.78
DG19wgmjc	58711.359925	i	21.49	0.17	21.78
DG19wgmjc	58712.215600	i	21.40	0.14	21.91
DG19wgmjc	58712.240520	i	21.52	0.14	22.02
DG19wgmjc	58712.291373	i	21.35	0.10	22.26
DG19wgmjc	58712.316480	i	21.30	0.10	22.17
DG19wgmjc	58712.369148	i	21.45	0.12	22.19
DG19wgmjc	58712.378929	z	21.55	0.12	22.19
DG19wgmjc	58713.258267	i	21.36	0.08	22.56
DG19wgmjc	58713.283160	i	21.59	0.08	22.78
DG19wgmjc	58713.338159	i	21.32	0.08	22.54
DG19wgmjc	58713.370145	i	21.54	0.07	22.81
DG19wgmjc	58716.185565	i	21.54	0.05	23.64
DG19wgmjc	58716.198218	z	21.62	0.05	23.46
DG19wgmjc	58716.217530	i	21.48	0.05	23.27
DG19wgmjc	58716.249927	i	21.46	0.05	23.24
DG19wgmjc	58716.281851	i	21.42	0.05	23.10
DG19wgmjc	58716.314735	i	21.46	0.07	22.92
DG19wxnjc	58710.282368	i	···	···	21.05
DG19wxnjc	58710.334265	i	···	···	20.35
DG19wxnjc	58710.335291	z	···	···	20.33
DG19wxnjc	58711.246513	i	···	···	21.20
DG19wxnjc	58711.247990	z	21.26	0.14	21.75
DG19wxnjc	58711.323118	i	21.43	0.13	22.05
DG19wxnjc	58711.324621	z	21.20	0.09	22.23
DG19wxnjc	58712.219736	i	21.78	0.19	21.95
DG19wxnjc	58712.221236	z	21.26	0.11	22.02
DG19wxnjc	58712.295533	i	21.64	0.16	22.02
DG19wxnjc	58712.297123	z	21.27	0.09	22.19
DG19wxnjc	58712.373291	i	21.59	0.12	22.29
DG19wxnjc	58712.374788	z	21.19	0.08	22.31

Table 5 continued

Table 5 *(continued)*

Internal Name	MJD	Filter	m	σ_m	$m_{\rm lim}$
DG19wxnjc	58713.262414	i	21.66	0.10	22.67
DG19wxnjc	58713.263892	z	21.29	0.06	22.81
DG19wxnjc	58713.343452	i	21.69	0.08	22.84
DG19wxnjc	58713.345519	z	21.23	0.05	22.77
DG19wxnjc	58716.190860	i	21.78	0.06	23.67
DG19wxnjc	58716.192927	z	21.35	0.03	23.48
DG19wxnjc	58716.255204	i	21.67	0.06	23.31
DG19wxnjc	58716.257275	z	21.27	0.05	22.90
DG19wxnjc	58716.320040	i	21.74	0.09	22.78
DG19wxnjc	58716.322111	z	21.26	0.07	22.56
DG19wynuc	58710.277547	i	...	...	21.10
DG19wynuc	58710.278567	z	...	...	20.74
DG19wynuc	58710.329439	i	...	...	20.11
DG19wynuc	58711.264626	z	...	...	21.28
DG19wynuc	58711.341745	z	...	...	21.54
DG19wynuc	58712.237831	z	...	...	22.11
DG19wynuc	58712.313817	z	...	...	22.30
DG19wynuc	58713.280501	z	22.81	0.21	22.87
DG19wynuc	58713.366851	z	22.65	0.20	22.79
DG19wynuc	58716.214279	z	22.74	0.16	23.13
DG19wynuc	58716.278622	z	22.77	0.19	22.93
DG19wynuc	58716.343389	z	22.87	0.20	23.02
DG19wynuc	58726.206674	i	23.24	0.15	23.71
DG19wynuc	58726.209543	i	22.76	0.08	24.00
DG19wynuc	58726.227477	i	22.54	0.07	24.10
DG19wynuc	58726.230348	i	22.71	0.06	24.14
DG19wynuc	58726.248539	i	22.73	0.07	24.19
DG19wynuc	58726.251423	i	22.73	0.06	24.24
DG19zcrpc	58710.275153	i	...	...	20.59
DG19zcrpc	58710.276173	z	...	...	21.10
DG19zcrpc	58710.328065	z	...	...	20.10
DG19zcrpc	58711.231432	z	...	...	21.76
DG19zcrpc	58711.235569	z	...	...	21.35
DG19zcrpc	58711.311879	z	21.96	0.19	22.10
DG19zcrpc	58712.204660	z	21.64	0.16	22.01
DG19zcrpc	58712.208802	z	21.96	0.20	22.05
DG19zcrpc	58712.280436	z	21.54	0.13	22.12
DG19zcrpc	58712.284576	z	21.90	0.16	22.21
DG19zcrpc	58712.358145	z	22.29	0.20	22.39
DG19zcrpc	58712.360780	i	...	...	20.94
DG19zcrpc	58712.362257	z	22.04	0.17	22.31
DG19zcrpc	58713.247322	z	21.96	0.11	22.69
DG19zcrpc	58713.251477	z	21.96	0.12	22.62
DG19zcrpc	58713.324292	z	22.34	0.13	22.92
DG19zcrpc	58713.329599	z	21.99	0.11	22.80
DG19zcrpc	58716.171752	z	22.33	0.08	23.49
DG19zcrpc	58716.177031	z	22.25	0.08	23.47

Table 5 continued

Table 5 *(continued)*

Internal Name	MJD	Filter	m	σ_m	$m_{\rm lim}$
DG19zcrpc	58716.236111	z	22.32	0.11	23.10
DG19zcrpc	58716.241409	z	22.35	0.12	23.03
DG19zcrpc	58716.300714	z	21.93	0.11	22.65
DG19zcrpc	58716.306173	z	21.90	0.10	22.74
DG19zoonc	58710.293513	z	···	···	20.85
DG19zoonc	58711.239722	z	···	···	21.73
DG19zoonc	58711.316028	z	···	···	22.27
DG19zoonc	58712.211452	i	···	···	22.19
DG19zoonc	58712.212956	z	22.00	0.20	22.10
DG19zoonc	58712.288735	z	22.03	0.21	22.06
DG19zoonc	58712.366493	z	···	···	22.45
DG19zoonc	58713.255616	z	21.97	0.11	22.75
DG19zoonc	58713.334931	z	21.93	0.12	22.60
DG19zoonc	58716.182342	z	22.21	0.07	23.55
DG19zoonc	58716.246714	z	22.11	0.09	23.10
DG19zoonc	58716.311507	z	22.14	0.12	22.84